Tectonophysics 875 (2024) 230263

Contents lists available at ScienceDirect

Tectonophysics

journal homepage: www.elsevier.com/locate/tecto

Integrating near-surface geophysical methods and remote sensing techniques for reconstructing fault-bounded valleys (Mellieha valley, Malta)

Luciano Galone [a,*], Fabio Villani [b], Emanuele Colica [a,c], Davide Pistillo [d], Paola Baccheschi [b], Francesco Panzera [e], Jesús Galindo-Zaldívar [f,g], Sebastiano D'Amico [a]

[a] Department of Geosciences, University of Malta, MSD2080 Msida, Malta
[b] Istituto Nazionale di Geofisica e Vulcanologia, Rome, Italy
[c] Research & Planning Unit, Public Works Department, Ministry for Transport, Infrastructure and Public Works, FRN1700 Floriana, Malta
[d] Dipartimento di Scienze della Terra, University of Rome "La Sapienza", 00185 Rome, Italy
[e] Department of Biological, Geological and Environmental Sciences, University of Catania, Italy, Catania, Italy
[f] Departamento de Geodinámica, Universidad de Granada, 18071 Granada, Spain
[g] IACT (CSIC- Universidad de Granada), 18071 Granada, Spain.

ARTICLE INFO

Keywords:
Malta
Near-surface geophysics
Remote sensing
Normal fault
Horst and graben
Red beds
Extensional tectonics

ABSTRACT

The island of Malta (central Mediterranean) is dissected by several WSW-trending fault-line valleys related to Miocene-Pliocene extensional tectonics. Some valleys host remnants of alluvial deposits that could provide information on possible Quaternary faulting, but the thickness of these deposits and their subsurface extent is poorly constrained. Our study aimed to investigate the structural configuration of the southern sector of the Mellieha valley, which is located in the north-west part of the island and is limited by the ENE-WSW general trending Mellieha and Ghadira faults, and their relation with a thin layer of infill sediments. We employed different near-surface geophysical techniques (electrical resistivity tomography, active and passive seismic methods, ground-penetrating radar), as well as remote sensing techniques (unmanned aerial vehicle digital photogrammetry and ground-based Light Detection and Ranging) to complement classic structural surveys. The valley structure has an asymmetric graben configuration, being bounded by a normal fault to the southeast (Mellieha Fault) and other to the north-west (Ghadira Fault). Our study provides insights of possible Quaternary fault displacements and revealed the presence of an additional fault splay, the previously unmapped NNW-dipping Mellieha Fault 2 at the south-eastern edge of the valley. Additionally, by integrating results from geophysical surveys, we estimated the thickness of the valley's recent deposits, being thicker towards the Mellieha Bay sector, with maximum values of 8–10 m. Our study aligns with the general model of horst and graben structuring with associated regional tilting since the late Miocene, and supports the hypothesis that some segments of NW-trending normal faults within the North Malta Graben exhibit Quaternary activity, although with minimal throw rates (<< 0.1 mm/yr).

1. Introduction

Normal faulting in extensional settings entails the generation of fault-bounded basins that may host *syn*-tectonic sediments, useful to provide constraints on the long-term evolution of their bounding faults. In continental settings, the sedimentary record in extensional basins is usually a fraction of the real amount of deposited material, due to the interplay between fault slip, regional vertical movements, erosional processes and discontinuous sedimentation (Gawthorpe and Hurst, 1993; Gawthorpe and Leeder, 2000; Burbank and Anderson, 2011). In these peculiar settings, particularly where slow fault slip rates are coupled with low amounts of sediment discharge, it becomes challenging to infer the fault evolution. Moreover, fault traces may be concealed by recent cover and their relation with *syn*-rift sediments may not be clear.

In these situations, near-surface geophysics is an essential tool for

* Corresponding author.
E-mail address: luciano.galone@um.edu.mt (L. Galone).

https://doi.org/10.1016/j.tecto.2024.230263
Received 27 June 2023; Received in revised form 19 February 2024; Accepted 27 February 2024
Available online 2 March 2024

imaging and locating subsurface faults and mapping the depth to the bedrock in tectonic basins (e.g., Butler, 2005; Everett, 2013). Among the various techniques, electrical resistivity tomography (ERT -e.g., Loke, 2002; Giocoli et al., 2015; Improta et al., 2010) is a powerful and efficient tool capable of providing electrical resistivity images of the subsurface that in most cases can be interpreted in terms of lithology and structural discontinuities. The advantage of this technique is the speed of execution and the fast-computing time of a robust model. However, caution is necessary to the interpretation, especially since the tomographic models are usually obtained through linearized inversion techniques that produce smooth resistivity images. Shallow active-source seismic profiling also yields excellent results in structural imaging (e.g., Gold et al., 2013; Stephenson et al., 2012), although the rough surface topography at the basin borders and very sharp velocity discontinuity in the near-surface hampers shallow reflection profiling in these settings. Refraction tomography in this case is a valuable imaging tool (e.g., Villani et al., 2015). It enables obtaining detailed subsurface velocity models that can in turn be compared with average lithological properties, due to the broad correlation existing between P-wave velocity and rock type (e.g., Sowers and Boyd, 2019). Among the passive seismic techniques, the Horizontal-to-Vertical Spectral Ratio method (HVSR) has gained increased popularity for its ease of application, particularly in the case of mapping the thickness of shallow low-velocity sediments overlying a rigid basement (e.g., Molnar et al., 2022; Paolucci et al., 2015). In the geological sciences, the emergence of technologies such as structure-from-motion photogrammetry, paired with the decreasing prices of unmanned aerial vehicles and Light Detection and Ranging (LiDAR) sensors (Colica et al., 2021a, Colica et al., 2021b; Bistacchi et al., 2022), together with other remote sensing techniques (e.g. Foody et al., 2009) has enabled to increase the efficiency of data collection through the construction and use of digital outcrop models, capable of providing large amounts of structural and stratigraphic information.

In this work, we present an application of combined near-surface geophysical surveying and digital outcrop models to reconstruct the geometry of a fault-bounded valley in the north-western sector of Malta, close to the village of Mellieha, between the Anchor and Mellieha bays (Figs. 1 and 2). The possibility of unraveling evidence of Quaternary fault activity in Malta is challenging because of the meager amount of preserved inland Quaternary sediments that may document any *syn*-rift deposition, and the poor exposures of continental deposits. Moreover, subsurface data constraining geometry and thickness of deposits filling fault-line valleys are generally lacking. This situation is further complicated by the massive urbanization of the island, as a result of which suitable sites for the study of continental sediments are reduced to a few valleys, mainly located in the north-western sector of Malta. The Mellieha fault-line valley represents a good site to test this multidisciplinary approach because it is one of the few that is fairly large in relation to the modest size of the island, and according to official geological maps, it contains thin remnants of continental sediments (Pedley, 1993). In particular, our focus is locating and imaging the shallow subsurface of the bounding faults, and estimating the thickness of recent continental deposits preserved in the valley. These data are used to infer the overall structure of the valley and the relation of the bounding faults with recent continental sedimentation. The latter in turn could provide some indication of the possible Quaternary fault activity. We additionally use digital outcrop analysis to map fracture patterns and to obtain information on fault geometry, and also use updated bathymetric datasets to infer the possible offshore extent of the surveyed faults. To our knowledge, this is the first application of an integrated geophysical and geomatic approach for structural geology studies in Malta. Since previous studies have been conducted only based on surface geological data, this work may contribute to a further understanding of the structures of fault-bounded valleys in Malta and their relations with its regional extensional tectonics.

2. Geological setting and the study area

The Maltese archipelago comprises three main islands (Malta, Gozo and Comino) located in the central Mediterranean, in the foreland of the Sicilian Thrust Belt. This region represents the uplifted part of a wide extensional crustal domain known as Pantelleria Rift (Fig. 1). The latter changes in strike from NW-SE to nearly W-E moving to the east and developed since the late Miocene with a major phase of crustal stretching during the Plio-Quaternary (Dart et al., 1993; Micallef et al., 2019). The Maltese archipelago is made of Oligocene-Miocene shallow water carbonates and deep-water clays forming a sub-horizontal to gently dipping multi-layer sequence (e.g., Pedley, 1993). The principal outcropping formations, from the oldest to the youngest, are the following: Lower Coralline Limestone Fm. (late Oligocene); Globigerina Limestone Fm. (early Miocene); Blue Clay Fm. (middle-late Miocene); Upper Coralline Limestone Fm. (late Miocene).

The generalized post-Miocene uplift explains the complete absence

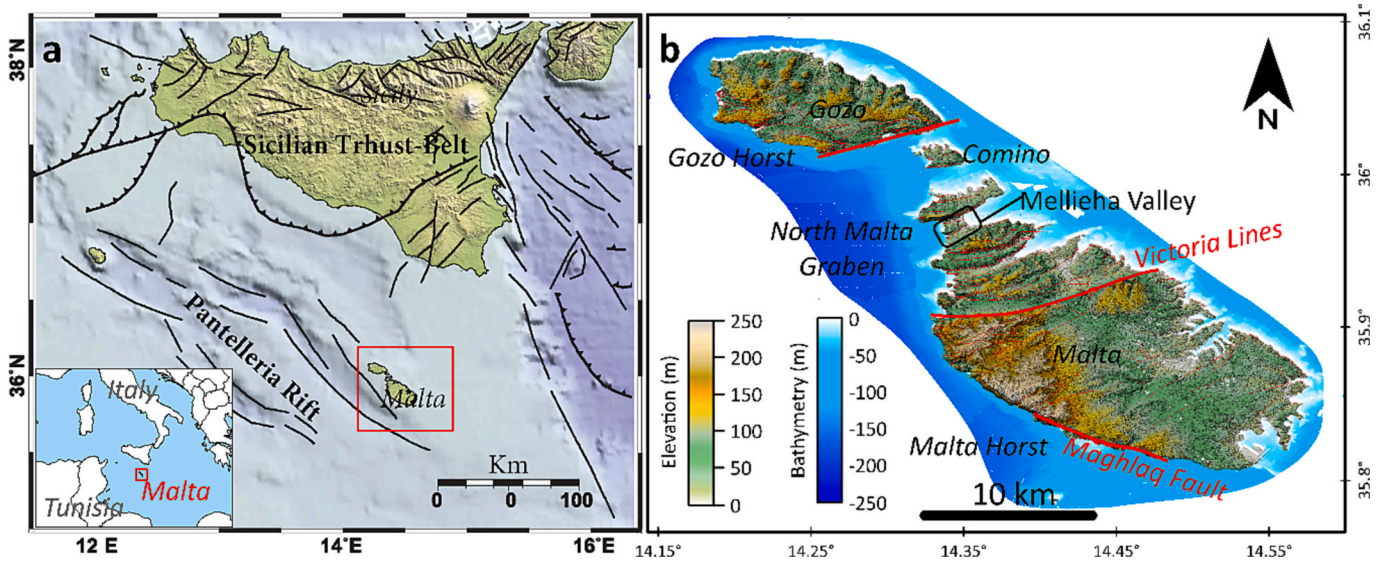

Fig. 1. Location map of the study area (Mellieha Valley). (a) Simplified structural map of the central Mediterranean (modified after Palano et al., 2012), and Malta location in the red square. (b) Topo-bathymetric map of the Maltese archipelago. The main structural features and the Mellieha Valley are shown. (For interpretation of the references to colour in this figure legend, the reader is referred to the web version of this article.)

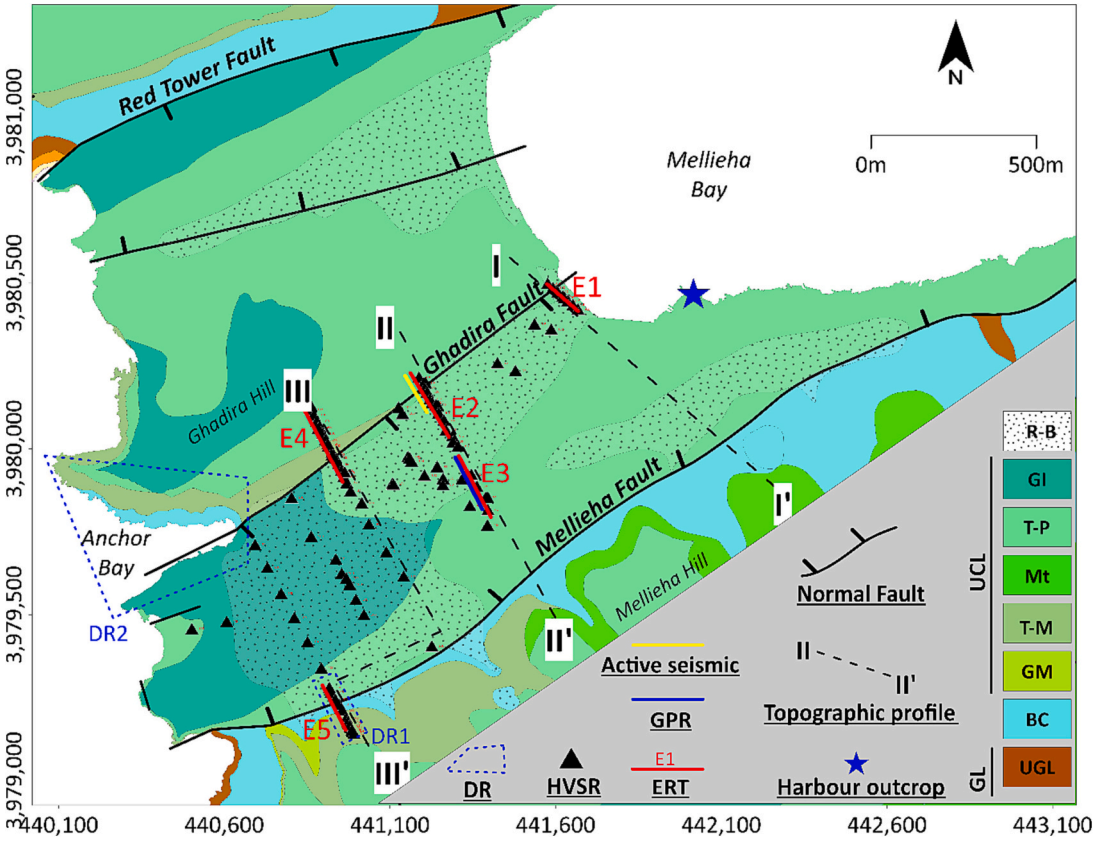

Fig. 2. Geological map of the Mellieha Valley study area and location of the main geophysical measurements. DR: digital reconstruction; HVSR: horizontal-to-vertical spectral ratio measurement; GPR: ground penetrating radar B-scan; ERT: electrical resistivity tomography; GL: Globigerina Limestone Formation; UGL: Upper Globigerina Limestone member; UCL, Upper Coralline Limestone Formation. Members of the UCL Fm. are indicated as follows: GM: Għajn Melel member; T-M: Tal-Mas member; Mt.: Mtarfa member; T-P: Tal Pitkal member; GI: Gebel Imbark member; BC: Blue Clay Formation; R-B: red beds. Coordinates in WGS84 system, zone UTM-33 N. (For interpretation of the references to colour in this figure legend, the reader is referred to the web version of this article.)

of Pliocene marine deposits as well as the scarcity of Quaternary sediments on the islands, which experienced different episodes of extensional tectonics that are well documented in the literature (e.g., Pedley et al., 1976; Pedley, 1993; Dart et al., 1993). This gave rise to two main tectonic trends that characterize the structural setting and geomorphology of the islands. The first trend is due to WSW-ENE trending normal faults that form a series of horst and graben structures, particularly well developed between Gozo and the northwestern part of Malta, and is responsible for the generation of the North Malta Graben (Fig. 1b). The second trend is related to NW-SE trending faults that are mostly developed in the southern sector of the island (e.g., Maghlaq fault in Fig. 1b, Bonson et al., 2007). Several works deal with the relations and timing of activity of these two fault systems (e.g., Dart et al., 1993; Bonson et al., 2007; Martinelli et al., 2019). The main phases of rifting began in the Late Miocene during the initial stages of the opening of the Pantelleria Rift and probably ceased during the Pliocene. Dart et al. (1993) inferred an almost uniform N-directed extensional regime affecting the archipelago since the Late Miocene. Martinelli et al. (2019) propose that the N-directed extension was preceded by a short-lived phase of WNW-directed extension in the Miocene. The vast majority of faults outcropping in the archipelago are considered currently inactive, whereas hints of recent faulting along some offshore segments mapped in the Gozo channel and to the west of the archipelago are reported by Micallef et al. (2019), who point out an active NE-extension affecting the study region.

According to some authors, specific segments of the major WSW-ENE faults outcropping in Malta (Victoria Lines fault, Fig. 1b) may have experienced some episodes of Quaternary activity as well (e.g., Villani et al., 2018). Putz-Perrier and Sanderson (2010) demonstrated, by means of several geological profiles, that the amount of extension accomplished by the WSW-ENE faults increases towards the North Malta Graben, so that the faults bounding this graben are the best candidates for Quaternary activity. Pedley et al. (1976) and Illies (1981) suggested that recent uplift to due fault activity may have affected the coastal regions to the north of Mellieha, attested by raised beach deposits and notches (see also Pedley, 2011).

The limestone backbone of these islands is dissected by a large number of fault-line valleys related to horst-and-graben parallel structures oriented mostly WSW-ENE (Alexander, 1988; Pedley, 1993). Being very close to the sea, and due to the limited dimensions of the drainage watersheds, the sediments laid by the short rivers were for the most part completely erased, particularly during the strong incision related to the sea level drop during the latest cold climatic phases (e.g., Hunt, 1997), leaving a discontinuous thin layer of fluvial and alluvial deposits. The preserved deposits are mostly confined in caves, or they constitute relics of conglomerates with a reddish matrix generally attributed to the Middle-Late Pleistocene (the so-called red beds; e.g., Hunt, 1997; Pedley, 2011).

The Mellieha valley (Fig. 2) is about 1.4 km wide and 1.5 km long. It represents a nearly symmetrical graben structure bounded by two structural highs exposing an almost complete section of the Upper Coralline Fm., locally showing the underlying top of the Blue Clay Fm. The official geological maps (Pedley, 1993; Continental Shelf Department, 2022) report at the borders of the graben two main WSW-ENE trending faults with opposite dips, which we name Mellieha fault (NNW-dipping) and Red Tower fault (SSE-dipping). In the central part of the graben, a small structural high is present, labeled as Ghadira hill, also made of Upper Coralline Fm. Our study is based on measurements

and observations conducted in the southern valley, which is limited by the Ghadira and Mellieha faults. We chose this site because of the documented presence of old alluvial sediments with a reddish matrix (*red beds*; see Pedley, 2011), whose thickness was unknown until now, that were laid down by an old fluvial network and subsequently deactivated by climatic changes and drastic sea level fluctuations occurred over the late Quaternary (e.g., Hunt, 1997).

3. Methodology

3.1. Proximity and remote sensing for digital reconstruction and structural data collection

To gain insight into the structural setting of the study area, we conducted geological observations and structural measurements in the areas where the primary basin-bounding fault zone is visible, as well as in Mellieha Bay (Fig. 2). To achieve this, we used a hybrid approach that combined traditional structural compass measurements with the creation of two digital reconstructions - DR1 and DR2 - using different methods.

DR1 was reconstructed over a rural road where fractures associated with the fault zone of the Mellieha Fault were observed, over the sector where the ERT E5 was performed (Fig. 2). Given the small size of the area, data acquisition was carried out using an iPhone 12 Pro max device equipped with a LiDAR sensor capable of reconstructing coloured and geo-referenced dense point clouds within a range of 5 m. The point cloud was analyzed by the Compass plugin (Thiele et al., 2019) installed in the Cloud Compare software v. 2.13 (Girardeau-Montaut, 2016), which allowed to digitize discontinuities interpreted as fractures and to obtain their strike. The digital dataset was validated by comparing the obtained fracture attitude values with compass measurements taken in a traditional manner. The results indicate that these two types of measurement provide azimuth values that can be considered very similar, as they usually fall within a range $< 5°$. For this reason, fracture mapping from digital models was useful to increase the density of structural data collection.

DR2 was performed in Anchor Bay (Fig. 2), where direct observation of the vertical cliff is challenging due to its sub-vertical morphology. Digital photogrammetry was used with photographs acquired using a DJI Phantom 4 Pro UAV, and 20 ground control points were measured by using a survey-grade Global Navigation Satellite System (GNSS). A total of 1953 images, with a pixel resolution of 5472×3648, were acquired using automated flight planning with the app Pix4D Capture with an 80% forward overlap and 70% side overlap. Images were inspected and those that were defective (e.g., out of focus or overexposed) were removed, to prevent processing failures. Subsequently, Structure from Motion processing was performed with Agisoft Metashape software v. 2.0.0, following the steps used by Colica et al., 2021a,Colica et al., 2023).

A third fault zone outcrop in the Mellieha harbor (Fig. 2) was measured by conventional structural methods. This outcrop is not mapped as a fault in official geological maps, and may represent the easternmost part of a second fault bounding the southern sector of the valley. Results were plotted on stereographic diagrams and rose diagrams for analysis and interpretation.

3.2. Geophysics

3.2.1. Electrical resistivity tomography

We acquired five ERT profiles at specific sections perpendicular to topographic scarps that hint at the presence of faults bounding the Anchor-Mellieha"s valley (Fig. 2). The aim was to characterize such geological structures and the very shallow sedimentary layers overlying the UCL Fm. The selection of the sites represents the best compromise between geological targets and logistical constraints imposed by the fragmentation of agricultural properties, as well as the presence of underground utilities and power lines that would cause unwanted anthropic noise.

Three ERTs were performed crossing the Ghadira Fault, one on the sandy beach deposits (E1) and two on the central section (E2 and E4). One ERT was set across the Mellieha Fault (E5) and another was conducted crossing perpendicularly a > 700 m-long escarpment parallel to the Mellieha Fault, where we suspect the presence of an unmapped fault (E3, roll-along array with an overlap of 50%).

We used a multichannel digital resistivity meter ELECTRA (Moho srl) featuring a waveform D/A converter with continuous current and voltage control, including feedback. The applied current during measurements was 10 mA. ERT's electrode location was measured using a GNSS system with sub-0.02 m accuracy and the altitudes corrected to the local geoid elevation were used for processing. Details of the ERT profiles are reported in Table 1 and locations in Fig. 2.

For all the locations, we acquired and compared the Wenner α and Schlumberger electrode arrays because they are sensitive to different electrical resistivity distributions in the subsurface. In particular, the Wenner α array is suitable for recovering stratified media with vertical resistivity contrasts, whereas the Schlumberger array probes a greater depth with respect to the Wenner α array. Results obtained in the field depend on the local conditions and the presence of some anthropic sources of noise (power lines) that in some cases affected data quality. For these reasons, in this paper, we show only the best inversion result for each profile. The processing routine consisted of identifying and filtering outliers in the raw data with a de-spiking technique. Data inversion was performed using RES2INV software v. 4.08 (Loke and Barker, 1996; Loke, 2002) based on the least squares linearized inversion technique with smoothing constraints. Models are parameterized as regular cells whose size depends on the electrode spacing and array type. Due to the fact that the number of model parameters exceeding the measured data makes the problem underdetermined, in the linearized inversion process a regularization parameter is introduced that determines the relative weight of data misfit and model misfit terms; the latter is a smoothing constraint that is automatically tuned during the inversion to avoid an overly smooth model or conversely a model containing unreasonable artifacts. The acquired datasets were processed by incorporating topography information. The forward model was established using a horizontal mesh size of 4 nodes to enhance the accuracy of apparent resistivity values and the finite-element method was employed for forward calculation, with the program automatically adjusting the grid size. We selected robust inversion constraints, which are less susceptible to highly noisy data and are particularly well-suited for delineating sharp boundaries, as expected at the R-B – UCL Fm. contact. The model assessment was done by taking into account the data quality and absolute percentage error, which is a function that describes the difference between recorded and calculated resistivity data. We also took into account the general feature of the resistivity distribution.

3.2.2. Horizontal-to-vertical spectral ratio

Ninety-six single-station ambient noise recordings were collected in the Mellieha valley. The extent of the measures is limited to areas where it was possible to access. We set up our measurements with the purpose of covering most of the valley, which was conditioned by its intense agricultural use. The seismic signals were analyzed to obtain the HVSR curves (Nakamura, 1989), computed as the ratio of the Fourier amplitude spectra between the quadratic mean of the horizontal components and the vertical component of the ambient vibrations. Following the approach of previous works in the Maltese islands (e.g., Vella et al., 2013; Leucci et al., 2021; Farrugia et al., 2016; Panzera et al., 2013), we used three Tromino (http://moho.world/), a compact three-component velocimeter with 24-bit digitizer, operating in the nominal frequency range of 0.1–300 Hz. Time series of ambient noise, having a length of 20 min, were recorded with a sampling rate of 128 Hz and, following the guidelines suggested by Bard and P.S (2004), they were divided into time windows of 20 s each not overlapping each other. A 5% cosine taper

Table 1
Summary of the ERT profiles presented in this study.

ERT	Location	N° electrodes	Interelectrode spacing	Array Length	Array type	Absolute Error	% of removed data
E1	Ghadira Fault – Beach deposits	32	2 m	62 m	Wenner α	11.8%	11.5%
					Schlumberger	18.1%	49%
E2	Ghadira Fault – Central sector	43	5 m	210 m	Wenner α	16.2%	7.1%
					Schlumberger	15.4%	61.0%
E3	Unmapped Fault – Central sector	64	5 m	315 m	Wenner α	31.1%	22.6%
					Schlumberger	18.7%	19.6%
E4	Ghadira Fault – Central sector	50	5 m	240 m	Wenner α	14.9%	10.9%
					Schlumberger	Too noisy data	
E5	Mellieha Fault – Southwest sector	64	2.5 m	155 m	Wenner α	13.2%	8.1%
					Schlumberger	Too noisy data	

was applied to each window and the Fourier spectra were calculated. The spectra of each window were smoothed using a Konno–Ohmachi window (Konno and Ohmachi, 1998) fixing the parameter b to 40. Finally, the resulting HVSR, in the frequency range 0.3–60.0 Hz, was computed by estimating the logarithmic average of the spectral ratio obtained for each time window, selecting only the most stationary and excluding transients associated with very close sources.

The results revealed an HVSR peak at frequencies between 1 and 2 Hz for the measurements made on the outcropping UCL Fm. and an additional peak at frequencies >5 Hz for the measurements made on the alluvial sediments (red beds) in the valley. Both peaks have amplitudes >2 units and correspond to an eye-shaped pattern in the spectral components (Fig. 3).

According to Bonnefoy-Claudet et al. (2006), the presence of pronounced peaks in the HVSR curve indicates impedance contrast at the selected site, given by a low average shear wave velocity (Vs) layer over a high Vs layer. In our case, the low-frequency peak is related to the Vs contrast between the relatively low Vs BC Fm. and the relatively high Vs GL Fm., as demonstrated in previous works (e.g., Panzera et al., 2012; Farrugia et al., 2016, 2021). On the other hand, we associate the high-frequency peak with the Vs contrast between the red beds and the UCL Fm., which has relatively high Vs (Panzera et al., 2012).

We used closely spaced single-station measurements to obtain smooth 2-D pseudo-tomographic sections of HVSR as a function of frequency and distance (using the code by Wathelet et al., 2020) that can be interpreted in a qualitative way as structural sections because they show the spatial continuity of seismic impedance surfaces characterized by consistently high HVSR values.

The use of HVSR peak frequencies for sedimentary thickness estimation is relatively common. The aforementioned peaks frequencies (f)

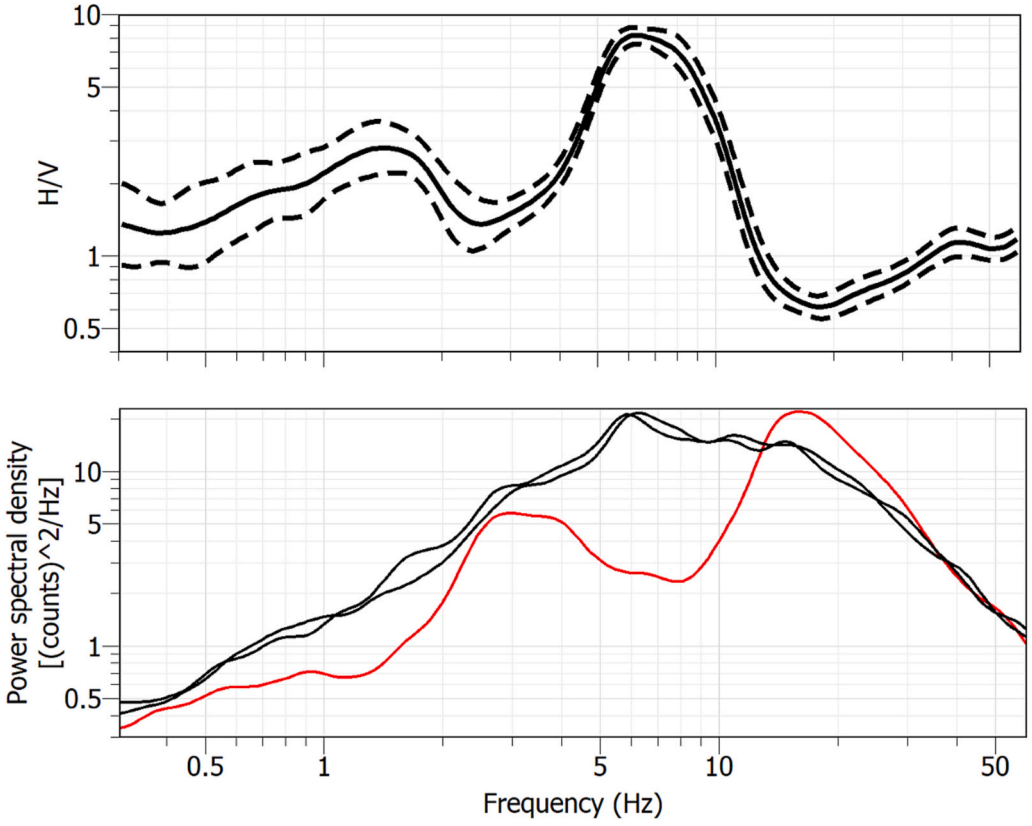

Fig. 3. Example of HVSR processing result. In the upper panel, the continuous black line represents the average HVSR function, whereas dashed black lines indicate standard deviations. The peak at frequency of around 1.5 Hz is associated with the resonance of BC Fm. over GL Fm. (e.g., Farrugia et al., 2016). The peak at 5.5 Hz is associated with the resonance of R-B over UCL Fm. The bottom panel displays the power spectral density of each component, with the red line denoting the vertical component and the black lines representing the horizontal components. Eye-shaped patterns (increase in horizontal components energy and decrease in vertical one) correspond to the frequency of HVSR peaks. (For interpretation of the references to colour in this figure legend, the reader is referred to the web version of this article.)

are related to the Vs of a layer with thickness (T) through the simple relationship f = Vs/(4 T), following the quarter-wavelength rule (Boore, 2003). One limitation of this approach is that a site-specific shear wave velocity profile is required for depth-conversion of these interfaces. To obtain insights into the distribution of red beds in the valley, we use the 1D assumption implicit in the f = Vs/(4 T) formula, by adopting Vs values for shallow soils obtained in other sites of the island with independent seismic measurements (e.g., Farrugia et al., 2016; Pischiutta et al., 2016; Villani et al., 2018).

3.2.3. *Active-source seismic profiling*

We acquired a high-resolution seismic profile crossing the fault scarp that bounds to the ESE the Ghadira hill, along ERT E2. We used 48 vertical geophones (4.5 Hz natural frequency) spaced 2 m and connected with 24-bit seismographs of Geode Geosystem (by Geometrics Inc.). The geophones we used have a nearly flat response from about 2 Hz up to 150 Hz, therefore they are suitable for shallow seismic profiling since they accurately record high-frequency direct and refracted P-waves (frequency range of 40–100 Hz) as well as surface waves (frequency range of about 5–30 Hz). The elastic energy was input into the ground by using a 5-kg sledgehammer with a spacing of 4 m. The handpicked first arrival travel times were inverted using a non-linear multi-scale refraction tomography code that uses a finite-difference eikonal solver and mixed Monte Carlo-Simplex optimization scheme: the main feature

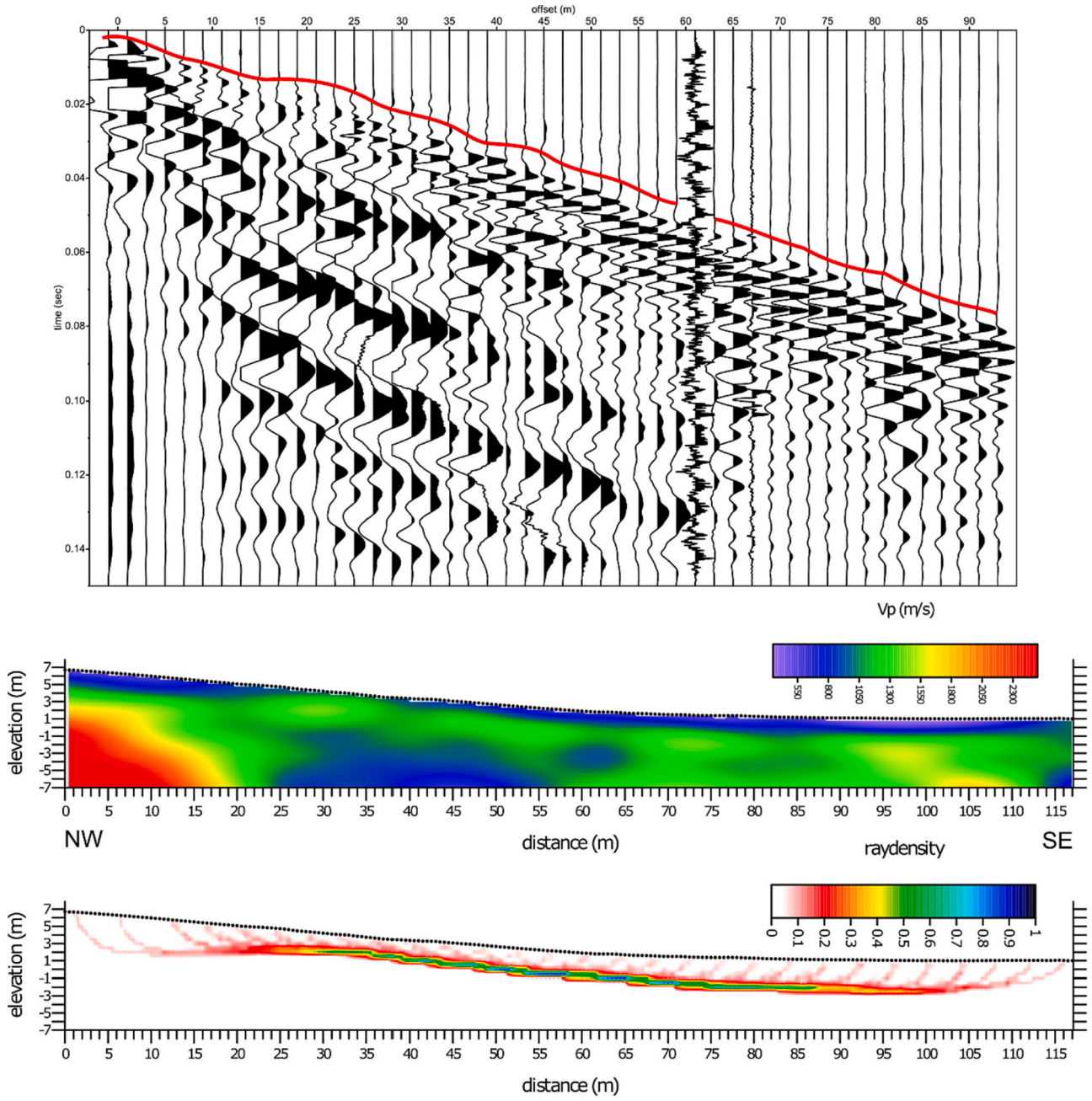

Fig. 4. Workflow of active-source seismic tomography used in this study. The upper panel shows a recorded common shot gather (CSG) collected during seismic profiling in the Mellieha valley (48 seismic traces, only amplitude normalization applied): the red line is the envelope of the picked first arrival travel times. The latter, together with traveltime readings from all other CSGs, are inverted through a non-linear algorithm (Herrero et al., 2000) to produce a 2D P-wave velocity model (central panel). The bottom panel indicates the seismic ray coverage (indicated as hit count within 1 m × 1 m cells) obtained by back-projecting rays from receivers to source. (For interpretation of the references to colour in this figure legend, the reader is referred to the web version of this article.)

of this inversion technique is that it does not require a starting reference model, which is obtained at the early stage of inversion through a massive search in the model space (Herrero et al., 2000). This approach was used on the island by Villani et al. (2018) for the shallow seismic imaging of the western sector of the Victoria fault. In this paper, we show a best-fit representative Vp model paired with a plot of ray coverage obtained with a back-ray tracing procedure (more details in Improta et al., 2002). The basic workflow of active-source seismic data is shown in Fig. 4.

Using the common shot gathers at the center and on both ends of the linear array deployment, we also apply the f-k analysis to extract the Rayleigh wave dispersion curve. This was done to try to infer the shear wave velocity of the red beds.

3.2.4. Ground penetrating radar

Ground Penetrating Radar (GPR) air-coupled Cobra Plug-In™ SUB-ECHO model (RadarTeam AB, Boden, Sweden) with a central frequency of 80 MHz was used to perform B-Scans in transects perpendicular to the major axis of the valley, with a sampling interval of 3.125 ns and 512 samples per trace over a time window of 600 ns, which corresponded to an approximate depth of 30 m in limestone with electromagnetic wave propagation velocities of 0.1 m/ns (Davis and Annan, 1989).

While this approach showed good results on the UCL Fm. in other sectors of the island (Colica et al., 2023), our results were mostly very noisy, probably due to the presence of medium and high-voltage power lines near the acquisition points. Despite this, a high-quality B-scan was obtained in the site of ERT E3, which presented good resolution and was included in this study. The data were processed using Prism2® software (RadarTeam, v2.7), applying time zero correction, background removal, bandpass filter and migration using the hyperbola fitting method (Colica et al., 2021b, Persico et al., 2019, Persico and Muci, 2023) obtaining a propagation velocity for electromagnetic waves of about 0.11 m/ns, and topographic correction was also applied (Fig. 5).

4. Results

4.1. Structural analysis from field data and digital outcrops

In the field, the fault outcrops are generally poorly preserved. We found evidence of an additional NNE-dipping fault, parallel to the main Mellieha fault, in the Mellieha Bay harbor (mean outcrop location E14.356785°, N35.96676°, blue star in Fig. 2). This fault displays a >1 m-thick NW-dipping damage zone with a mean trend of about N220°-225° (also including small antithetic, SE-dipping faults) and vertically displaces the UCL Fm. of about 2 m (Fig. 6). This outcrop pinpoints the easternmost part of a subdued normal fault structure, suggested by the occurrence of a >700 m-long escarpment parallel to the main Mellieha fault and that we investigated by means of near-surface geophysics.

On an outcrop located in the southern part of Mellieha Valley over the Mellieha Fault, where DR1 was performed (mean coordinates E14.34548°, N35.95516°), several high-angle fractures and small faults were found, suggesting the presence of a thick fault zone with a general east-west trend and dipping to the north (Fig. 7).

The DR2 model allowed for precise measurements and images of the exposure of the Ghadira fault, which bounds the homonymous hill to the south, along the coast of Anchor Bay (Fig. 8). The main fault dips to the ESE with a relatively high angle ($>70°$) and is roughly parallel to the limit of Anchor Bay, suggesting structural control in the shape of the bay. The damage zone associated with the fault is approximately 20 m wide and contains at least one minor synthetic fault. The main fault puts in contact the members of the UCL Fm: Tal-Pitkal, in the footwall block, and Gebel Imbark, in the hanging wall block. The throw measured in the photogrammetric model is around 20 m, taking into account the position of the Gebel Imbark member base on both sides of the fault zone.

4.2. Geophysical sections

We describe the results of the geophysical sections along topographic

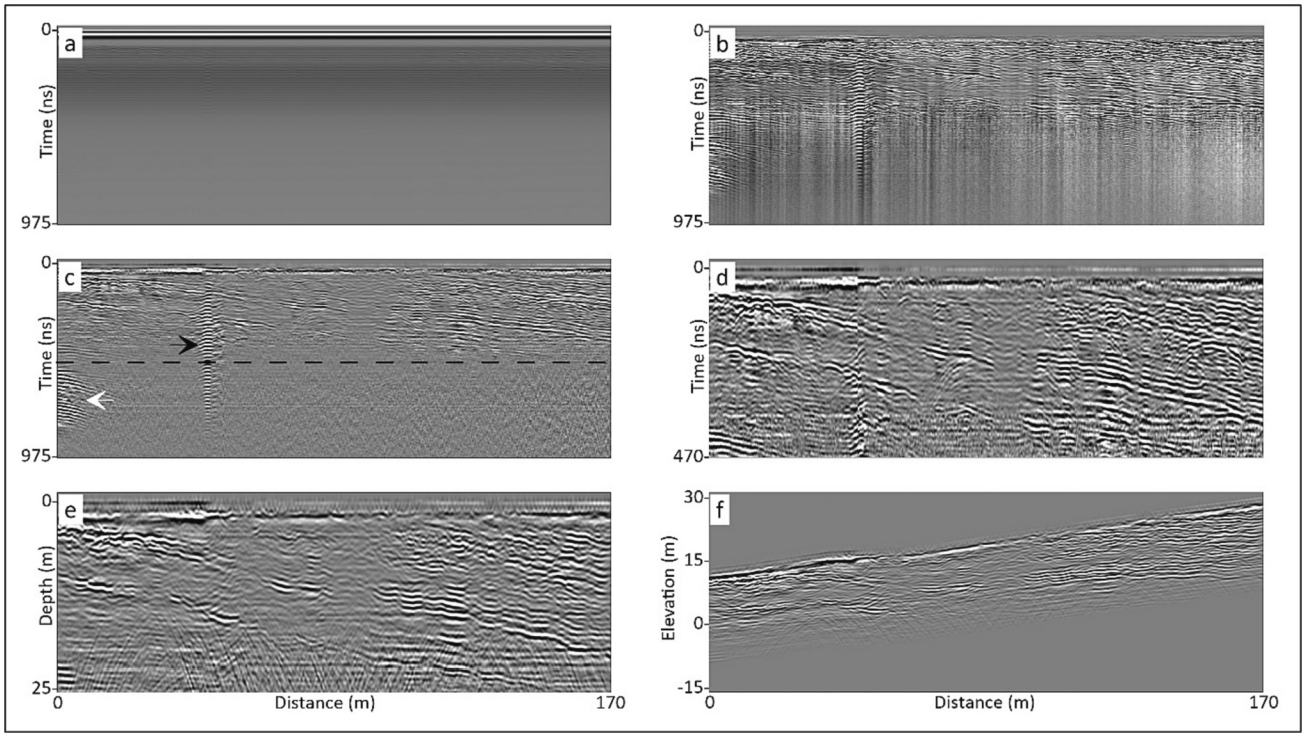

Fig. 5. GPR B-scan processing workflow. (a) Raw data. (b) Background removal. (c) Bandpass filter. The white arrow indicates the right part of a hyperbola (indicating probably a karstic feature), the black arrow indicates a ringing effect, dash black line indicates the maximum signal penetration. (d) zoom of the more superficial part of the radargram. The portion with the ringing effect is deleted. Oblique interfaces are evident, interrupted at the central part of the radargram. (e) migrated B-scan. (f) Migrated b scan with the topographic correction. Elevation refers to the sea level.

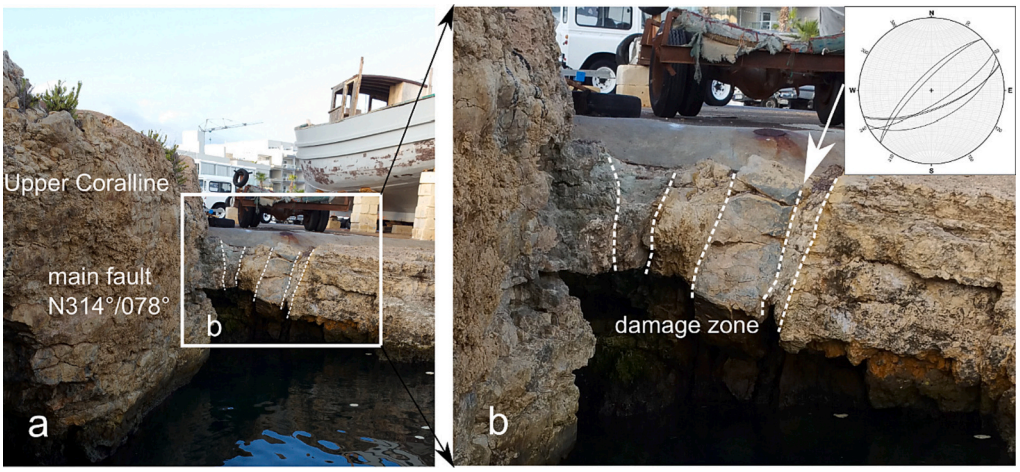

Fig. 6. Evidence of the NE termination of the fault bounding the Mellieha bay to the south-east. (a) NW-dipping normal fault zone (N314°/078°) affecting the Upper Coralline Fm. at the Mellieha Harbor (Dawret it-Tunara, coordinates E14.356949°, N35.966816°). (b) Detail of the small-displacement fault damage zone. Fault attitude notation is dip direction/dip angle.

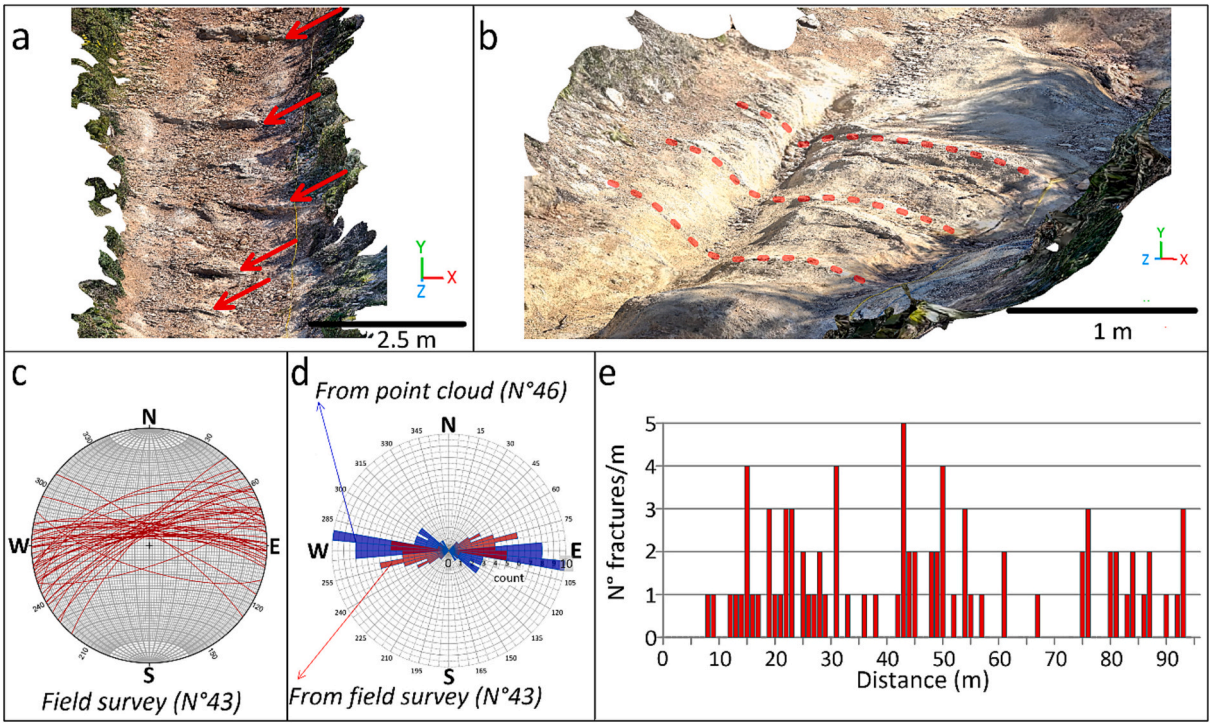

Fig. 7. Surface structural data collected along the Mellieha Fault. (a) and (b) Details of digital model DR1 reconstructing an outcrop over a rural road across the Mellieha fault zone, co-located with ERT profile E5. Red arrows and dash lines indicate meso-faults. (c) Stereplot indicating small meso-faults measured in the field. (d) Rose diagram indicating the azimuthal distribution of faults measured in the field (red petals) and those mapped from the digital model (blue petals). Count ranges from 0 to 10. (e) Bar plot of fracture density per meter surveyed along a 96 m-long section of the profile. Two main clusters of fractures are found at 15–30 m and 40–55 m, respectively. (For interpretation of the references to colour in this figure legend, the reader is referred to the web version of this article.)

profiles I-I′, I-II' and III-III' (location in Fig. 2) from the north-eastern to the south-western part of the Mellieha valley (Figs. 9–11).

The geophysical section along the I-I′ profile was conducted on the beach deposits of Mellieha Bay (Fig. 9). It consists of an ERT profile (E1) (Fig. 9b) and a HVSR frequency tomographic plot (Fig. 9c), where the colour palette indicates the amplitude of HVSR as a function of distance (x-axis) and frequency (y-axis). These results were obtained from eight ambient seismic noise measurements spaced 15 m apart along the E1 (black triangles on Fig. 9b and c), whose position is shown on the topographic profile (Fig. 9a).

The ERT E1 (Fig. 9b) revealed relatively low resistivity values ranging from 1 to 15 Ωm. In this section, distinct domains were identified, characterized by pronounced resistivity gradients. A thin, approximately 1 m-thick horizontal layer with relatively high resistivity values was observed in the shallowest portion, while a thicker domain of high resistivity values was observed towards the northern part (x = 0–30 m). Between x = 30–120 m, a zone with relatively low resistivity values (< 4 Ωm) was identified, characterized by a distinct lower boundary that dips towards the northwest. An additional domain of relatively high resistivity values deepening to the northwest appeared below this zone, between depths of −8 and − 15 m.

The HVSR values obtained along the co-located E1 (Fig. 9c) ranged

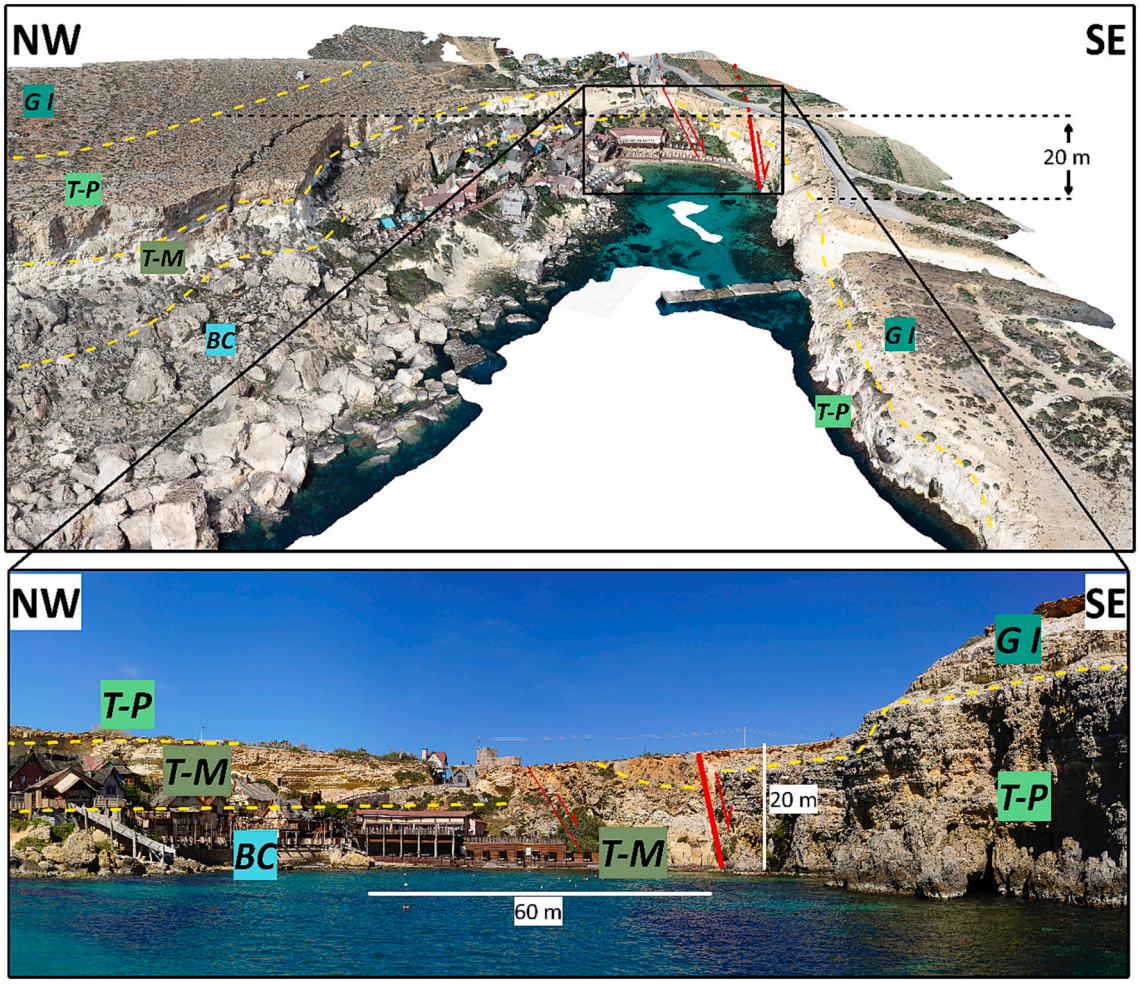

Fig. 8. Anchor Bay. Top panel, digital outcrop model DR2 interpreted from Anchor Bay. The throw measured on the base of the GI member is approximately 20 m. Bottom. Panoramic picture of the fault zone. The main fault is indicated by a thicker red line. The dash-yellow line indicates the approximate stratigraphic boundaries. BC: Blue Clay Formation; T-M: Tal-Mas member; T-P: Tal-Pitkal; GI: Gebel Imbark member. (For interpretation of the references to colour in this figure legend, the reader is referred to the web version of this article.)

from 0.5 to 9 units in the profile drawn based on ambient noise recordings. Interpolation of the values obtained at each station revealed two interfaces: one at frequencies below 2 Hz throughout the profile, and another at frequencies between 4 and 10 Hz approximately, extending from x = 30 m to the end of the section.

The observed discontinuities in both the ERT and HVSR sections around x = 30 m were interpreted as block displacement due to the Ghadira fault, with the NW block acting as the footwall block. The overall low resistivity values were interpreted as due to the proximity of the sea, where the saline water may saturate the pore rocks and sediments, thus strongly increasing the conductivity. The relatively high thin resistivity layer at the surface was identified as dry sand, while the thick high resistivity domain between x = 0–30 m corresponds to a very shallow UCL Fm. The relatively low resistivity zone may indicate the presence of non-lithified sedimentary infill material (indicated in Fig. 2 as red beds, R-B). A gentle dip of the base of these deposits towards the fault can be observed. The high-frequency HVSR interface was interpreted as low-velocity deposits above the UCL Fm., which is characterized by higher Vs values that produce a positive seismic impedance contrast. The abrupt interruption of this interface at x = 30, coinciding with the lateral change of ERT resistivities, supports the interpretation of the presence of a fault (Fig. 9c). On the other hand, the low-frequency interface was interpreted as the relatively low-Vs BC Fm. above the higher-Vs GL Fm. We do not see a clear step in the lower impedance contrast (Fig. 9c) because the associated wavelength (about 350 m, considering a Vs of 400 m/s) is too large compared to the small fault displacement. Our HVSR interpretation aligns with previous studies in Malta, where HVSR peaks around 1 Hz were interpreted as due to the BC Fm. - GL Fm. contact (e.g., Panzera et al., 2012; Villani et al., 2018; Farrugia et al., 2016, 2021). HVSR results are discussed in more detail in Section 4.3.

The geophysical sections in profile II-II' were carried out in the central sector of the Mellieha valley (Fig. 10). We acquired one ERT (E2) and a co-located P-wave refraction tomography in the NW sector, and an ERT (E3) and a co-located radargram in the SE sector (Fig. 10a).

The electrical resistivity values obtained in the ERTs (Fig. 10b) range from 20 Ωm to over 1500 Ωm. In both sections, a shallower layer with average thicknesses ranging from 2 to about 10 m was observed, with resistivity values <150–200 Ωm. Underneath this shallow layer, a zone of higher resistivity (up to 1500 Ωm) was recognized separated from the overlying layer by a high-gradient thin belt. In the case of the ERT located to the NW (E2), the geometry of this interface is sub-horizontal, and at x = 0–20 m, high resistivity values (>600 Ωm) are also present at the surface. On the other hand, the interface in the ERT located to the SE (E3) is more irregular and exhibits a stepped geometry, with a general northwest dip.

The P-wave tomography obtained from the seismic profile overlapping to E2 (Fig. 10c) shows values of Vp < 600–800 m/s in the shallow 3–5 m, and > 1400 m/s at greater depths. In particular, a discontinuous near-surface low-Vp layer (350–700 m/s), with a

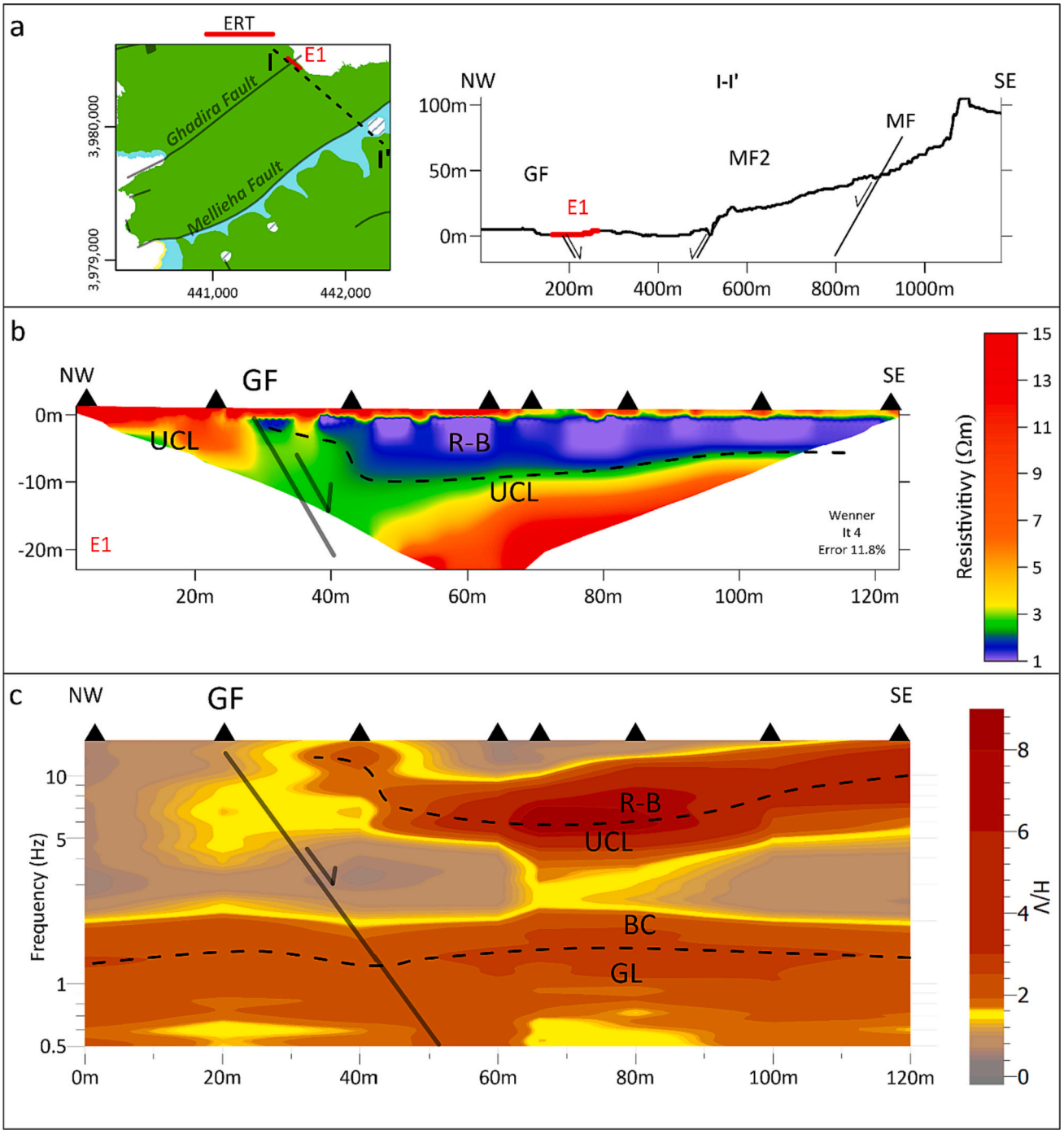

Fig. 9. Results of geophysical surveys along transect I-I′. (a) location of the surveys (top-left inset), and the topographic profile with inferred fault locations (top-right panel). (b) ERT model from profile E1 with simplified interpretation. (c) HVSR distance vs. frequency section obtained from ambient noise single station measurements (represented by black triangles in b and c), in which colour scale indicates the intensity of HVSR amplitude (see details in Section 3.2.2).

thickness of about 1–2 m, is visible at x = 0–15 m and x = 50–110 m along the profile, and which we interpret as the red beds. In the deep sectors, the Vp values are homogeneous between x = 0 and 20 m, while they show drastic lateral changes with lower Vp values in the central and southern parts of the profile. The lateral change is particularly noticeable between x = 20 and 60 m, where a high Vp body (> 2300 m/s) is in lateral contact with a layer showing a Vp around 1300 m/s. Using the common shot gathers at the centre and on both ends of the linear array deployment, from f-k analysis we extracted and stacked four Rayleigh wave dispersion curves, which are defined between 20 Hz and 65 Hz and display at least 3 modes. The thin layer of red beds as inferred from P-wave tomography is about 1–2 m-thick, and unfortunately, it is not resolved by the MASW. Therefore, we did not invert the dispersion curve to extract a Vs profile, but it is possible to deduce the presence of an outcropping high-velocity layer with Vs 600–800 m/s compatible with UCL Fm. This velocity range is in agreement with previous work in Malta (Pischiutta et al., 2016; Villani et al., 2018; Iannucci et al., 2020).

In the radargram (Fig. 10d), we observe that the shallower sections (approximately the uppermost 5 m) exhibit variable amplitude and nearly continuous reflectors parallel to the topographic surface, which depict smooth interfaces with a non-uniform thickness distribution. We interpret these shallow units as well-bedded sediments (red beds). Below

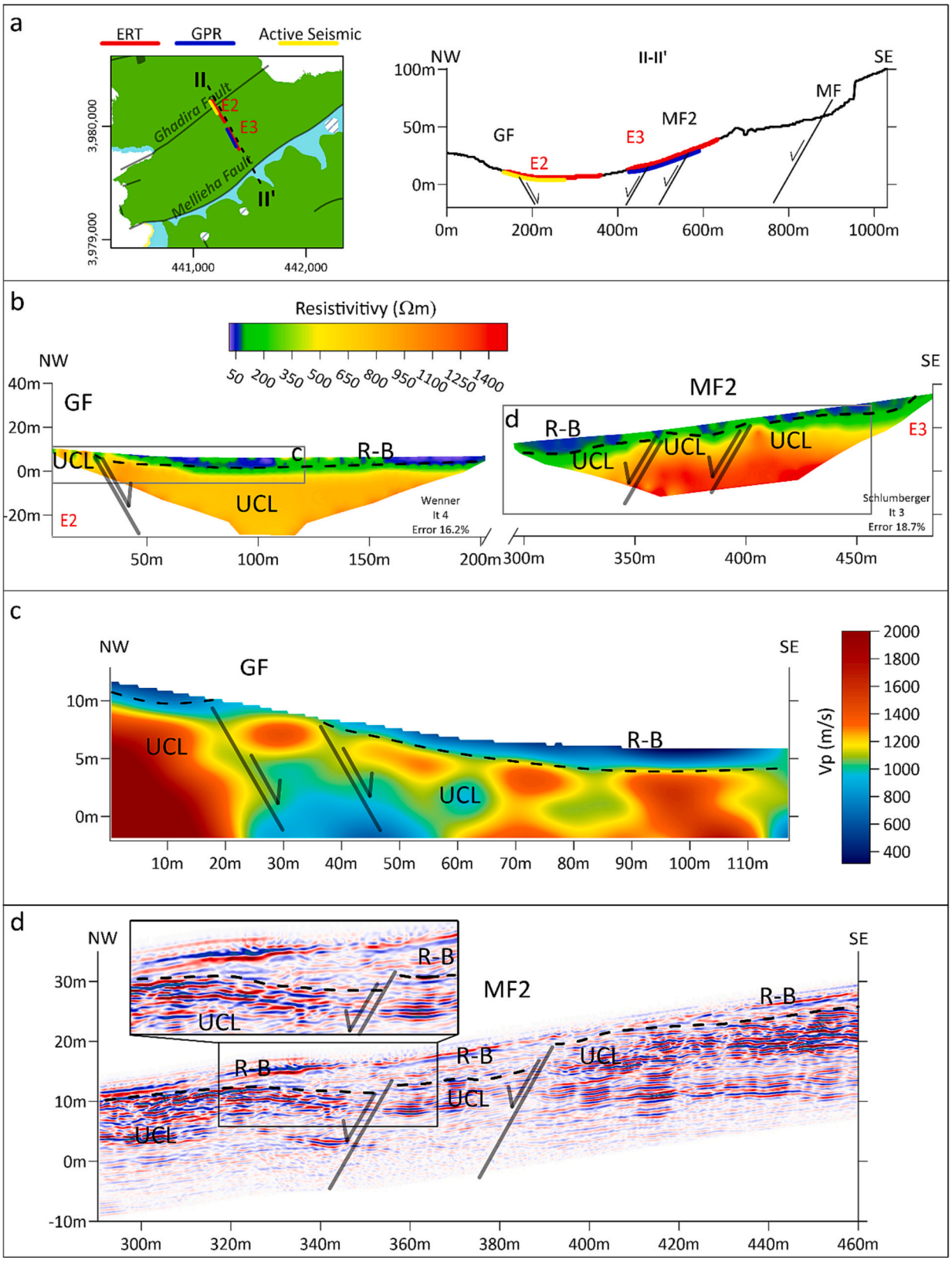

Fig. 10. Results of geophysical surveys along transect II-II'. (a) location of the surveys (top-left inset), and the topographic profile with inferred fault locations (top-right panel). (b) ERT models from sections E2 and E3 with simplified interpretation. (c) 2D Vp model from active-source seismic profile; (d) GPR section (see details in the text).

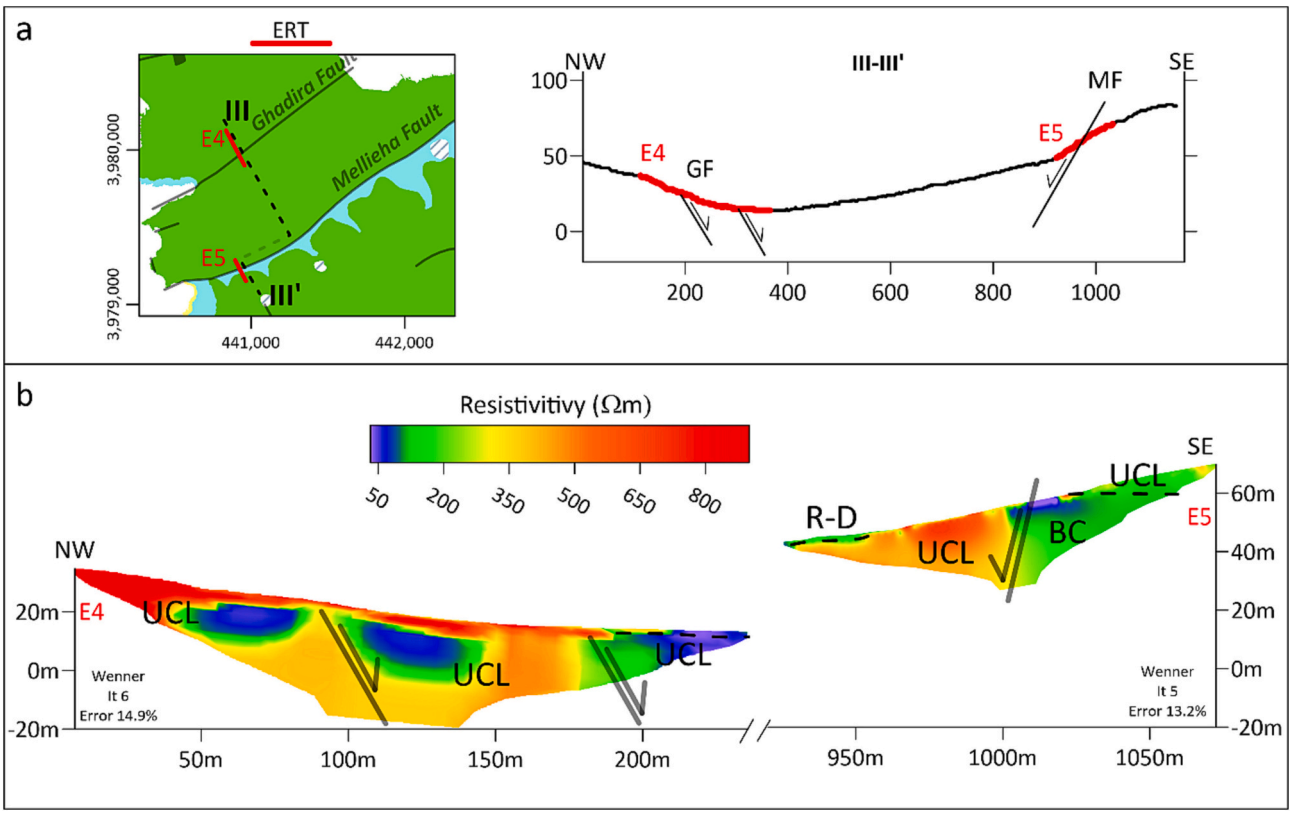

Fig. 11. Results of geophysical surveys along transect III-III'. (a) location of the surveys (top-left inset), and the topographic profile with inferred fault locations (top-right panel). (b) ERT models from sections E4 and E5 with simplified interpretation (see details in the text).

them, high-amplitude reflectors are present suggesting the occurrence of deeper interfaces, which vanish at depths close to 15 m. These domains are interpreted as the UCL Fm. The UCL Fm. interfaces are interrupted and vertically displaced at approximately x = 350 and 390 m, which we interpret as due to normal faulting. In the northwest sector, the UCL Fm. interfaces show a gentle couterslope dip that hints for a fault-controlled backtilt. In this sector, above the UCL Fm., the shallow sediments display a wedge shape thickening towards the southeast (zoomed in on Fig. 10d). In the central and southeast sectors of the radargram, the UCL Fm. interfaces exhibit a gentle dip parallel to the surface slope.

The discontinuities in the geophysical profiles show consistent features that were interpreted as fault zones with prevailing normal kinematics, in accordance with the local geological setting. The zones with low seismic velocities and strong lateral velocity gradients shown in the P-wave tomography were interpreted as fault zone fractures affecting the bedrock. We interpreted the shallow layer with low Vp (around 600-800 m/s) as due to the occurrence of unlithified alluvial deposits (red beds) with a thickness of about 2–3 m. In the SE sector, the GPR section (Fig. 10 d) is consistent with the presence of a normal fault zone and red beds at the same location as suggested by the ERT E3 (Fig. 10b).

The geophysical section along profile III-III' consisted of two ERT profiles (E4 and E5) that cross the most pronounced topographic breaks and the location of the mapped faults at each valley margin (Fig. 11a). Both profiles are nearly parallel and display a lateral offset of 350 m measured along the valley direction.

Resistivity values from the ERT E4 (Fig. 11b) carried out on the north-western margin of profile III-III' displayed resistivity values >600 Ωm at the surface. At depth, a stratified zonation with values around 70 Ωm immediately below the shallow resistive layer was observed, with values increasing at depth. Low resistivity values below 5 m depth were interpreted as more conductive facies of the UCL Fm., as the BC Fm. is found deeper (e.g. Mantovani et al., 2013).

Two faults have been interpreted where the resistivity shows evident lateral changes, one at approximately x = 150 m and the other at approximately x = 200 m. The latter is placing the red beds deposit in the SE in contact with the UCL Fm. The interpretation of two faults aligns with the DR2 observations at Anchor Bay, where two faults were also interpreted (see Fig. 8).

In ERT E5 section (Fig. 11b), located in the southwest part of III-III', a marked lateral discontinuity of resistivity values was observed in its central sector. There, the UCL Fm., with resistivity values >200 Ωm and extending towards the valley, is in lateral contact with the upper part of the BC Fm., which has resistivity values <200 Ωm. Between them, a steeply dipping normal fault zone was interpreted, consistent with the presence of fractures mapped in the DR1 (Fig. 7) and the fault reported in the official geological map (Continental Shelf Department, 2022). On the surface, the SE block shows resistivity values reaching a minimum of 10 Ωm, increasing up-slope. In the shallow part of the NW block, a small cradle-shaped zone with relatively lower resistivity values was observed and interpreted (supported by field observations) as the recent sedimentary deposits made of reddish alluvial deposits with clayey sandy matrix, which can be defined as typical red beds like those described by Hunt (1997) in nearby sites in Malta.

4.3. *Estimating the thickness of the alluvial cover in the Mellieha Valley*

In order to assess the extent and thickness of inferred red beds in the investigated Mellieha valley, we used results from geophysical profiles (ERTs 1–5 and the active seismic profile) together with the best-quality HVSR results. ERT models define the occurrence of red beds as a very thin shallow layer of relatively low resistivity (< 50 Ωm), while evidence of red beds from P-wave tomography is given by a shallow layer displaying Vp of about 350–700 m/s. HVSR results showed two distinct patterns that in our interpretation likely reflect differences in the distribution of the recent valley infill sediments in the study area. The seismic stations located directly on the UCL Fm. or above extremely thin

soils present only one HVSR peak with amplitudes >2 at frequencies between 1 Hz and 2 Hz. On the other hand, stations located in the central sector of the valley show a second peak at higher frequencies (> 5 Hz), which decreases in frequency towards the northernmost sectors of the valley, i.e., towards the Mellieha Bay.

Low-frequency peaks are related to Vs velocity contrast between the BC Fm. and the GL Fm. (e.g., Panzera et al., 2012; Farrugia et al., 2016, 2021). No clear spatial trends were found in the peak of f0 of the single station measurements. On the other hand, we can assume that the high-frequency peak is related to the Vs velocity contrast between the recent alluvial deposits (red beds) and the valley bottom, made of UCL Fm., which displays higher velocities (Vs around 800–900 m/s according to Panzera et al., 2012 and confirmed by our dispersion curve extracted from the active seismic profile deployment).

We assumed that the unconsolidated sediments (red beds) constitute a layer having Vs in the range of 150–250 m/s laying over UCL Fm. Such velocity range is justified by previous studies: for instance, MASW surveys across the Victoria fault revealed shallow red beds with Vs in the range of 120–150 m/s and weathered top UCL Fm. and GL Fm. capped by thin soils with Vs of about 240 m/s (Villani et al., 2018). Such velocity ranges, when using the eq. T = Vs/4F, where T is the sediments thickness and F is the selected resonance frequency, provide T values that display small differences, because of the very high value of F. Values of T obtained using this formula from the HVSR measurements were integrated with thickness values from ERT and active seismic data. The whole dataset was used to obtain the map in Fig. 12: this map shows the calculated recent sediment thickness obtained by interpolation with a kriging algorithm and a subsequent low-pass Gaussian smoothing filter.

From this map, it appears that the thickness of the recent deposits increases from the central part towards the northern-central part of the Valley and at Mellieha Bay beach, with values around 8–10 m. At the same time, thickness values decrease towards the valley sides and to the SW. The thicknesses determined for the SW sector of the valley are <1 m.

In the study area, it is difficult to find good exposure of red beds because they are usually intensively exploited for agricultural purposes. During some road work excavations (April 2022), we were able to document the occurrence of red beds consisting of crudely bedded alluvial gravels mixed with angular limestone pebbles and abundant reddish sandy matrix, supporting the results of geophysical measurements (Fig. 12, inset photo).

5. Structural model

Structural analysis of the outcrops confirmed the Mellieha normal fault bounding the SE edge of the valley, which has a high angle with NNW dip (about 70°). The geophysical section along profile III-III' (Fig. 11b) gives a picture of the physical characteristics of the subsoil in this sector, showing a decrease in electrical resistivity with minimum values in the fault zone, which puts in lateral contact the top of the BC Fm. with the UCL Fm. The occurrence of a conductive fault zone separating clays (BC Fm.) and marly limestones (UCL Fm.) results in a smooth and wide electrical response in the ERT profile, from which it is difficult to infer the precise attitude of the fault, which anyway appears as a steep structure. Therefore, for the interpretation, we take advantage of the ancillary surface data. The extent of the fault zone as mapped from ERT results is supported by fracture analysis performed in the field and using digital outcrops DR1 (> 20 m; Fig. 7). Fracture density peaks constrain the fault location. The associated fractures display dominant trends of N075°-080° and N095°-100°: the first trend is consistent with the trend of the inferred main fault, whereas the other one may be related to secondary fractures occurring in the fault zone.

Towards the central sector of the Mellieha valley, a second escarpment, on which the UCL Fm. outcrops, hints at the presence of a second

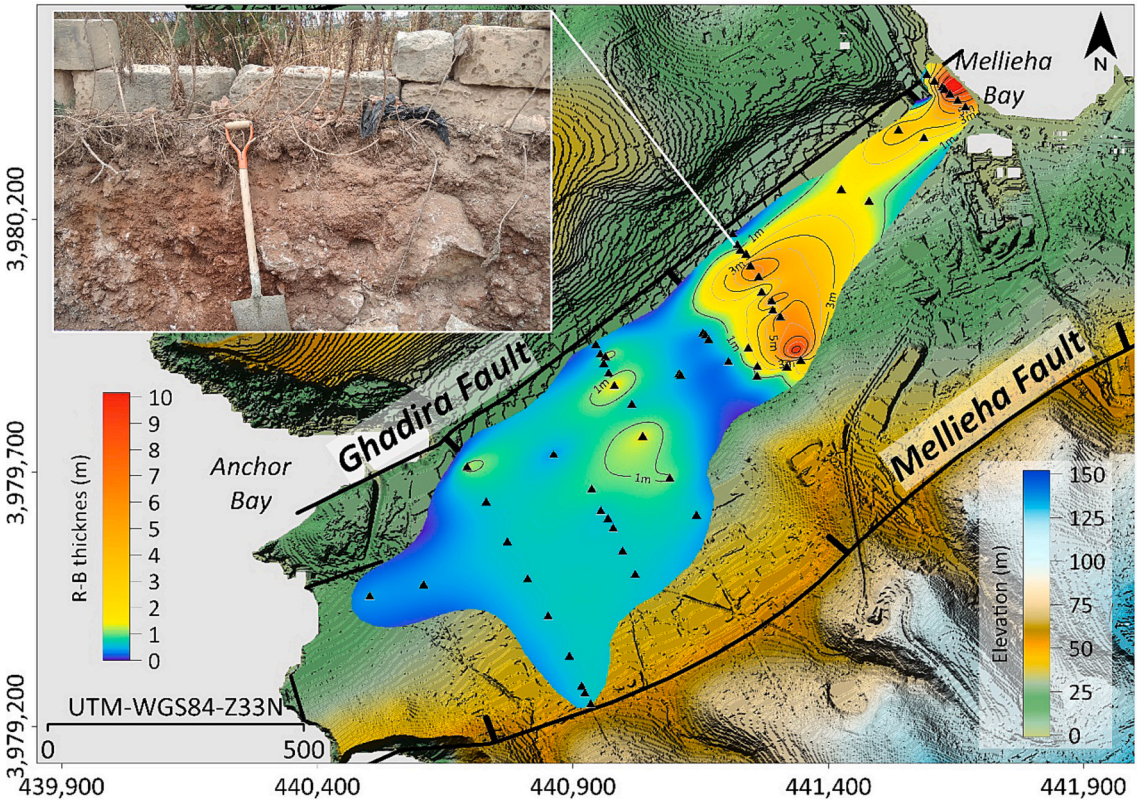

Fig. 12. Contour map of the quaternary (red beds) deposits thickness inferred from ambient noise survey. Black triangles represent the HVSR measurements employed. Detail of quaternary alluvial sediments (red beds) trapped in the Mellieha valley and temporarily exposed during road works (picture 28 April 2022; approximate location is indicated). (For interpretation of the references to colour in this figure legend, the reader is referred to the web version of this article.)

fault along the south edge of the valley, not reported so far in geological maps. Geophysical sections along profile II-II' (Fig. 10b and d) present evidence of this fault, which would be formed by a relatively complex zone with high angle normal faults dipping towards the valley, synthetic with the main Mellieha fault, and which in this work we call Mellieha Fault 2 (MF2). ERT E3 and radargram indicated a vertical displacement of about 5–10 m affecting the UCL Fm. Outcrops of this fault can be observed in its NW prolongation at Mellieha Bay, where high ENE-dip values were measured (>68°), confirming results similar to those of the Mellieha Fault (Fig. 6).

In the Anchor Bay the Ghadira fault zone, which bounds the NW edge of the valley, is well exposed. In this sector, a throw of about 20 m for the Ghadira fault has been calculated by digital outcrop analysis of DR2 (Fig. 8). Geophysical data along profile III-III' (ERT E4) in the sector confirms the location of the faults (Fig. 11b). Towards the center of the valley, geophysical sections on profile II-II' (Fig. 10b and c) show evidence of the fault both as a decrease in electrical resistivity values and a decrease in P-wave velocity associated with a sharp lateral velocity contrast between high-Vp (2300 m/s) and low-Vp layers (about 1300 m/s). The geophysical data along profile I-I' (Fig. 9b and c), acquired over the beach deposits of Mellieha Bay, also show evidence of faulting in this sector, and the minimum throw of the fault here is estimated to be about 8 m.

In general, the valley structure inferred by integrating our near-surface geophysical data, the collected structural measurements and information on Tertiary formations thickness from geological maps, is summarized in Fig. 13: the valley appears as an asymmetric graben. The NW edge is bounded by a SE-dipping high-angle normal fault (Ghadira fault, GF), while the SE edge is bounded, in its south-western sector, by a master fault (Mellieha fault, MF) and, from the center of the valley towards the Mellieha bay, also by a second NW-dipping synthetic normal fault (labeled Mellieha Fault 2, MF2).

The map of red beds thickness (Fig. 12) provides hints on the sedimentary and tectonic processes that took place in this area during the Quaternary. We point out that, according to literature data (e.g., Dart et al., 1993; Putz-Perrier and Sanderson, 2010), most of the fault activity in Malta took place during the late Miocene-Pliocene, although some authors have suggested that there may have been more recent tectonic

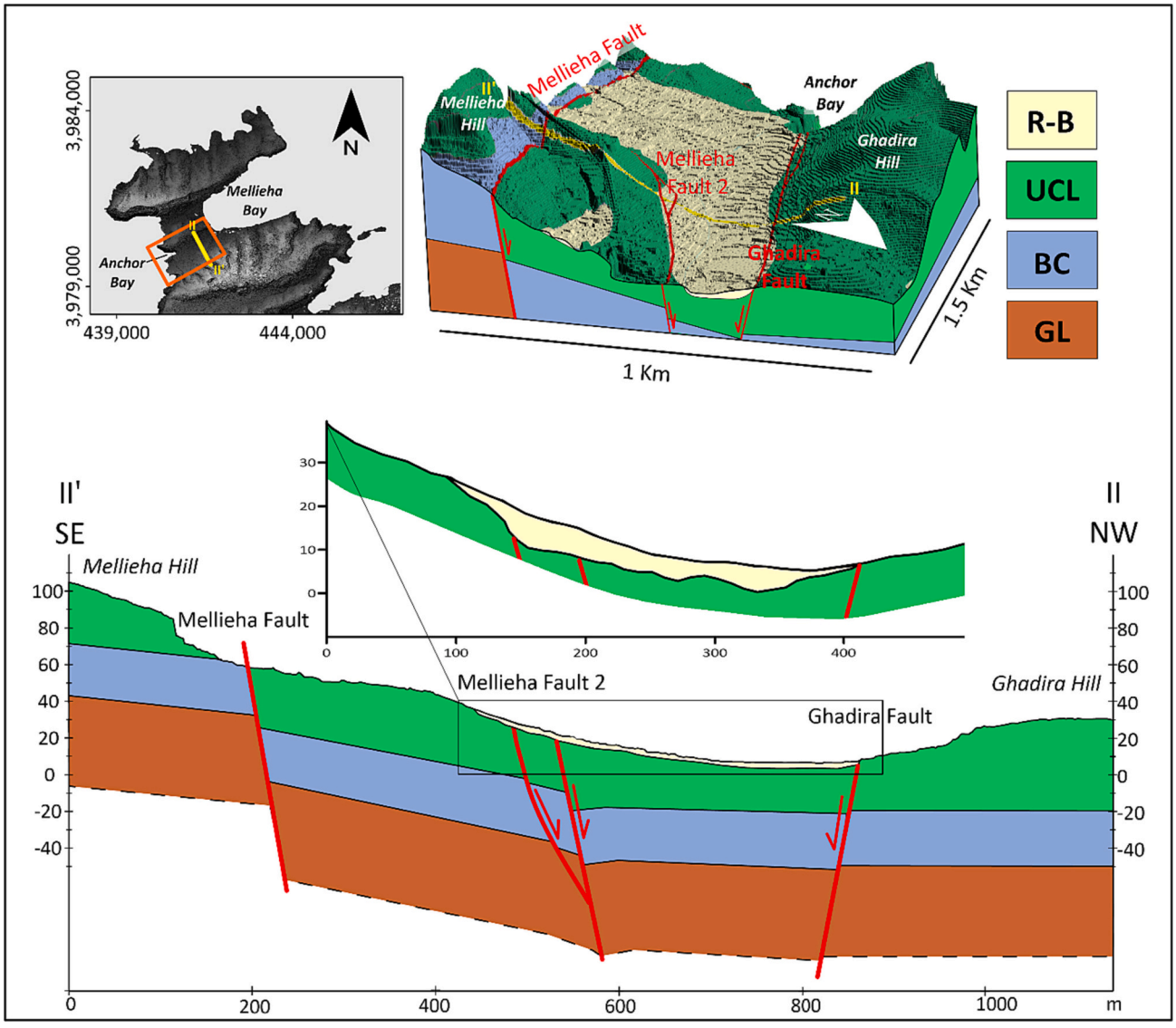

Fig. 13. Schematic block diagram (top) and geological cross section (bottom) illustrating the structure of the valley under study. The orange rectangle in the inset map represents the block diagram location. Elevations are referred to the sea level. The yellow line represents the geological cross-section location. GL: Globigerina Limestone Formation; BC: Blue Clay Formation; UCL: Upper Coralline Formation; R-B: Recent deposits (red beds). (For interpretation of the references to colour in this figure legend, the reader is referred to the web version of this article.)

displacements in this sector of the island (e.g., Pedley et al., 1976; Illies, 1981). The increase in recent sedimentary deposit thicknesses towards the NE of the valley can also be partly explained by a larger accommodation space due to a general topographic slope inherited from the regional NE-tilting of the island, which mostly occurred from the Miocene up to the mid-Pliocene (Pedley, 2011). This tilting concurred to strip away sediments from the southwestern uplifted blocks, which now expose mostly bare rock, and convey them in the distal parts of the NE-flowing river valleys.

The apparent asymmetry in the thickness of the deposits along profile I-I′ (Figs. 9b and c and 12), with greater thicknesses towards the NE boundary of the valley, may be due to the recent tectonic activity of the Ghadira fault. Similarly, we found that the infill deposits thicken in the central part of the valley, along profile II-II', where the activity of the Ghadira fault is likely paired with slip along the Mellieha Fault 2. The thickness of these deposits could then be used as a proxy for the minimum Quaternary activity of the northern section of these fault segments. Maximum sediment thickness values are observed in the central and north-western parts of the valley towards the Mellieha Bay (8–10 m). These values are very small compared to the duration of the Quaternary period (2.5 Ma), implying very low sedimentation rates possibly due to low sediment discharge coupled with long periods of erosion. Dating these deposits would provide essential information on the geological evolution of this sector of the Maltese archipelago. As a working hypothesis, we can restrict the time window to the past 0.5–0.8 Ma, taking into account the possible Middle Pleistocene age of the red beds inferred by Pedley (2011) based on their similarities with the fanglomerates outcropping close to the Maghlaq fault (see a discussion on the age of these deposits in Villani et al., 2018). For the same reasons, the decrease in thickness towards the SW of the valley could indicate less activity in this segment consistent with a decrease in Quaternary fault displacement. In any case, the amount of fault displacement inferred from soil thickness data is highly speculative and subject to uncertainty.

Thanks to the use of bathymetric data (10 m/pixel) provided by the Maltese Planning Authority, it was possible to track the faults that limit the Mellieha Valley in the offshore sector. Fig. 14 displays a seafloor slope map, where the colour palette represents the magnitude of the seafloor gradient at each point. The slope values are calculated using digital bathymetric data and are expressed in degrees, ranging from 0° to 90° (see Moore et al., 1993).

The Anchor Bay seafloor shows steep slopes, while the slopes are smoother towards the Mellieha Bay sector, following the regional NE topographic tilt of the island. In the Mellieha Bay, a scarp parallel to the inland Mellieha Fault can be observed, accompanied by a deepening of the seafloor, which we interpret as the offshore extent of the Mellieha Fault 2, revealed in this study. Thus, the southern limit of Mellieha Bay would be composed of two high-angle, stepped and parallel normal faults.

Similarly, morphological evidence from bathymetry indicates that the Ghadira Fault extends northeast into Mellieha Bay at around 20 m b.s.l., where a nose-shaped high is present. The latter depicts the offshore extent of the Ghadira Hill horst block. The maximum vertical displacement of this fault was found in Anchor Bay, estimated at around 20 m in the DR2 model. By taking into account the bathymetric data towards the southwest of Anchor Bay, it seems that this outcrop defines the southwest limit of the fault because no clear extent of the fault offshore is visible. At the same time, geophysical results indicate smaller displacements, of the order of 8 m, in the NE sector, where the Mellieha Bay beach deposits thicken towards the fault. This greater displacement on the south-western tip of the Ghadira Fault could be explained by the transfer of displacement to the adjacent and parallel faults to the NW (including the Red Tower fault), which exposes the GL Fm. and LCL Fm. in the footwall, and as a differential regional uplift of the northeast part of the island during the Miocene.

Therefore, our geophysical, photogrammetric, structural and bathymetric data support the general model of the northern sector of Malta being an extensional domain forming horst and graben structures that host at places some continental deposits, as in the case of the Mellieha Valley. Normal faulting along closely spaced and WSW-trending segments was active in the framework of an asymmetric

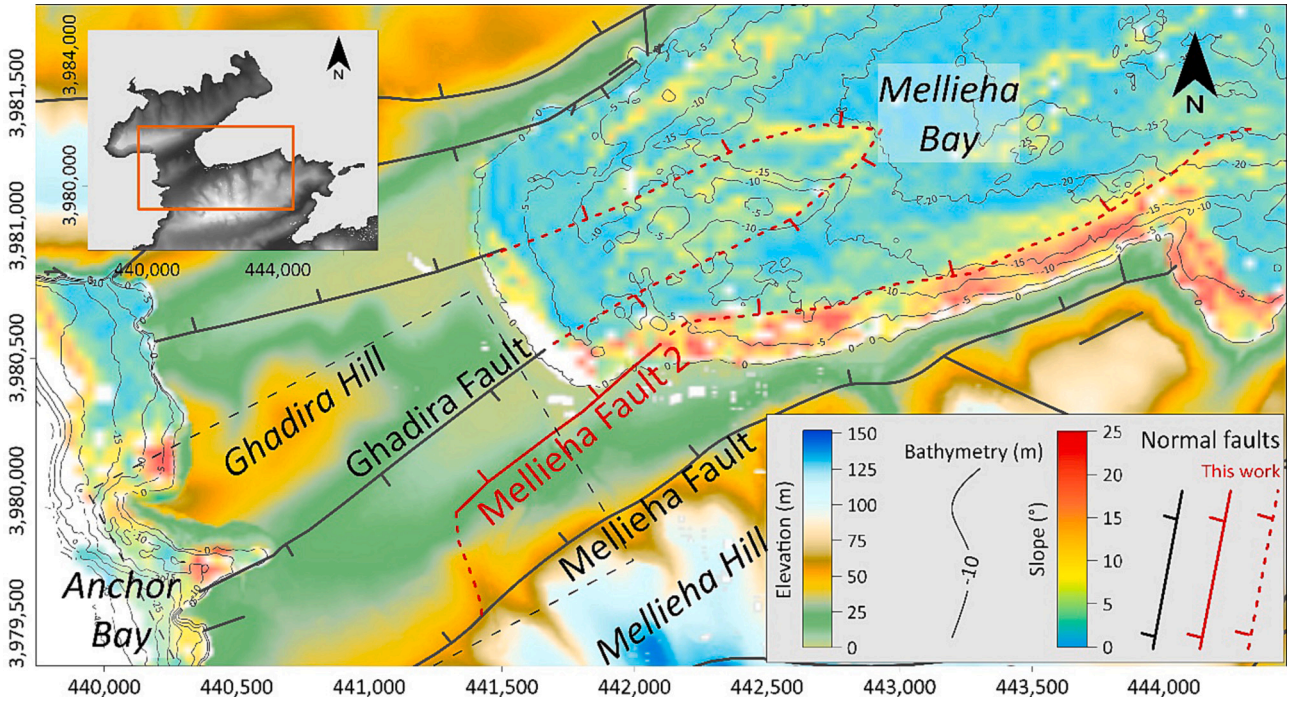

Fig. 14. Topographic and slope map illustrating the extent of inferred seafloor faults based on morphological information. On land, colors indicate elevations. In the offshore part, the colour scale indicates terrain slopes, while contour lines indicate bathymetry. Solid red lines represent faults determined in this study, while dashed red lines represent those inferred from morphological information. The orange rectangle in the top-left map represents the general location of the survey area. Coordinates in WGS84-UTM-Z33N. (For interpretation of the references to colour in this figure legend, the reader is referred to the web version of this article.)

regional tilting, likely related to the late Miocene to recent opening of the Pantelleria Rift (e.g., Dart et al., 1993). Following the end of the main phase of uplift (which likely took place in the final part of the Pliocene), some localized activity affected a few fault segments, including those bounding the Mellieha graben, as pointed out by our geophysical profiles and the uneven distribution and thickness of red beds within the valley. The inferred resulting fault displacements achieved in the Quaternary are quite small, probably not exceeding a few meters. This novel result is the first in this sector of the island of Malta and is in broad accordance with some previous inferences (e.g., Pedley et al., 1976; Illies, 1981) on the recent tectonic activity in the area surrounding the North Malta graben. We point out that Micallef et al. (2019) mapped several fault scarps offshore, with dominant trends NW-SE and WSW-ENE, and they infer that most of them show evidence of activity in the past 20 ka, in the framework of a current NE-extension. Some of these scarps represent the offshore prolongation of onshore faults, as in the case of the NE tip of the Mellieha fault. Therefore, our results are consistent with these findings, and support the hypothesis that NW-trending normal faults within the North Malta Graben display Quaternary activity and they may be still active, although with very low throw rates (<< 0.1 mm/a).

Further investigations and additional data, including an accurate estimation of the age of the continental deposits preserved in the Valley, may clarify some aspects of the recent geological evolution of the area.

6. Conclusions

In this multidisciplinary study, we used various geophysical and remote sensing methods to obtain a detailed image of the geological structure of the southern sector of the Mellieha valley, located within the North Malta Graben, in the northern part of the island of Malta. We employed electrical resistivity tomography, active and passive seismic techniques and ground penetrating radar, as well as remote sensing techniques such as UAV photogrammetry, ground-based LIDAR and bathymetry data.

The results enabled us to identify the structural settings of the valley, including the presence of a previously unmapped fault, which we have named the Mellieha fault 2. The valley structure has an asymmetric graben configuration, where a splay of two synthetic faults at the south-eastern boundary (the Mellieha Fault and the Mellieha Fault 2) and a fault at the north-western boundary (the Ghadira Fault). Analysis of the bathymetric data allowed us to track the offshore extent of the Ghadira fault, Mellieha fault and Mellieha fault 2, evidenced by high slope gradients in the seafloor topography in the Mellieha Bay.

We estimated vertical displacements of the Ghadira Fault of around 20 m in Anchor Bay and about 8 m in Mellieha Bay. This difference in vertical displacements could be explained by the differential uplift of the NE sector of the block representing Ghadira Hill, as well as by displacement transfer to the adjacent faults to the north (including the Red Tower fault). Additionally, we estimated the thickness of the recent deposits (so-called red beds) in the valley, showing a trend of increasing thickness towards the Mellieha Bay sector, partly following the regional topographic slope. Our findings suggest a certain wedging with increasing thicknesses towards the Ghadira Fault and Mellieha Fault 2, indicating possible activity of those segments of the fault during the Quaternary. The Quaternary activity of these faults is consistent with recent studies that outline some recent fault scarps offshore in the North Malta Graben, close to our study area.

Overall, the different geophysical and remote sensing methods we used allowed us to obtain a detailed image of the geological structure of the area. These findings are significant for better understanding the structure and recent tectonic dynamics in the Mellieha Valley area, providing insights into the recent evolution of the North Malta Graben, which is an important regional morphostructure developed in response to the opening of the Pantelleria Rift. Moreover, this work highlights the benefits of using a multidisciplinary approach in structural studies that combines field data collection, shallow geophysical prospecting and remote sensing.

CRediT authorship contribution statement

Luciano Galone: Visualization, Validation, Software, Methodology, Investigation, Formal analysis, Data curation, Conceptualization, Writing – review & editing, Writing – original draft. **Fabio Villani:** Validation, Supervision, Software, Project administration, Methodology, Investigation, Funding acquisition, Formal analysis, Data curation, Conceptualization, Writing – review & editing, Writing – original draft. **Emanuele Colica:** Software, Methodology, Investigation, Writing – review & editing. **Davide Pistillo:** Investigation. **Paola Baccheschi:** Investigation, Writing – review & editing. **Francesco Panzera:** Software, Investigation, Writing – review & editing. **Jesús Galindo-Zaldívar:** Investigation, Writing – review & editing. **Sebastiano D'Amico:** Validation, Supervision, Project administration, Investigation, Funding acquisition, Formal analysis, Conceptualization, Writing – review & editing, Writing – original draft.

Declaration of Competing Interest

The authors declare the following financial interests/personal relationships which may be considered as potential competing interests:

F. Villani reports financial support was provided by National Institute of Geophysics and Volcanology. S. D'Amico reports financial support was provided by Malta Council for Science and Technology and the INTERREG V A–Italy-Malta Capitalization Programme.

Data availability

Data will be made available on request.

Acknowledgments

S. Amoroso, A. Antonioli, L. Cantore, A. Cuoghi, D. Farrugia, P. Galea, G. Manzi, D. Di Naccio, P. Iregbeyen, A. Mercuri, L. Piccolini, M. Pischiutta, and A. Rovelli provided precious support during some early field surveys performed in the study area. We would also like to thank Ritienne Gauci (University of Malta) for her useful comments about the geology and structural data interpretation of the area. Topobathymetric information from ERDF 156 data, (2013), Developing National Environmental Monitoring Infrastructure and Capacity, Planning Authority was used in this work.

Two anonymous reviewers provided insightful comments that helped us improve the quality of the manuscript.

Part of the field activities were conducted within the framework of the INGV Project "Ricerca Libera" BR2019.23 ("Unveiling silent faults in low strain-rate regions through the integration of high-resolution geophysical and seismological analyses," Principal Investigator: Fabio Villani), the project "Multi-disciplinary monitoring system for resilient management of coastal areas (REMACO)," financed by the INTERREG V A–Italy-Malta Capitalization Programme (local P.I., S. D'Amico), and the IPAS+ (Internationalisation Partnership Awards Scheme), supported by the Malta Council for Science and Technology (https://mcst.gov.mt/).

References

Alexander, D., 1988. A review of the physical geography of malta and its significance for tectonic geomorphology. Quat. Sci. Rev. 7, 41–53. https://doi.org/10.1016/0277-3792004. 188)90092-3.

Bard, P.Y., P.S, August 2004. The SESAME project: an overview and main results. In: Proceedings of the InProc. of 13th World Conf. on Earthquake Engineering, Vancouver, BC; Vancouver, pp. 1–6.

Bistacchi, A., Mittempergher, S., Martinelli, M., 2022. Digital outcrop model reconstruction and interpretation. In: Bistacchi, A., Massironi, M., Viseur, S. (Eds.), 3D Digital Geological Models. https://doi.org/10.1002/9781119313922.ch2.

Bonnefoy-Claudet, S., Cornou, C., Bard, P.Y., Cotton, F., Moczo, P., Kristek, J., Fäh, D., 2006. H/V Ratio: a tool for site effects evaluation. Results from 1-D noise simulations. Geophys. J. Int. 167, 827–837. https://doi.org/10.1111/J.1365-246X.2006.03154.X.

Bonson, C.G., Childs, C., Walsh, J.J., Schöpfer, M.P.J., Carboni, V., 2007. Geometric and kinematic controls on the internal structure of a large normal fault in massive limestones: the Maghlaq fault, Malta. J. Struct. Geol. 29, 336–354. https://doi.org/10.1016/J.JSG.2006.06.016.

Boore, D.M., 2003. Simulation of ground motion using the stochastic method. Pure Appl. Geophys. 160, 635–676.

Burbank, D.W., Anderson, R.S., 2011. Tectonic Geomorphology: Second Edition. https://doi.org/10.1002/9781444345063.

Butler, D.K., 2005. 2005. Society of Exploration Geophysicists, Near-Surface Geophysics, ISBN 1560801719.

Colica, E., D'Amico, S., Iannucci, R., Martino, S., Gauci, A., Galone, L., Galea, P., Paciello, A., 2021a. Using unmanned aerial vehicle photogrammetry for digital geological surveys: case study of selmun promontory, northern of Malta. Environ. Earth Sci. 80, 1–14. https://doi.org/10.1007/S12665-021-09846-6/TABLES/3.

Colica, E., Antonazzo, A., Auriemma, R., Coluccia, L., Catapano, I., Ludeno, G., Persico, R., 2021b. GPR investigation at the archaeological site of Le Cesine, Lecce, Italy. Information 12 (10), 412. https://doi.org/10.3390/info12100412.

Colica, E., Galone, L., D'Amico, S., Gauci, A., Iannucci, R., Martino, S., Pistillo, D., Iregbeyen, P., Valentino, G., 2023. Evaluating characteristics of an active coastal spreading area combining geophysical data with satellite, aerial, and unmanned aerial vehicles images. Remote Sens. (Basel) 15. https://doi.org/10.3390/rs15051465.

Dart, C.J., Bosence, D.W.J., McClay, K.R., 1993. Stratigraphy and structure of the Maltese graben system. J. Geol. Soc. Lond. 150, 1153–1166. https://doi.org/10.1144/gsjgs.150.6.1153.

Davis, J.L., Annan, A.P., 1989. Ground-penetrating radar for high-resolution mapping of soil and rock stratigraphy 1. Geophys. Prospect. 37 (5), 531–551.

Everett, M.E., 2013 Near-Surface Applied Geophysics 1–399, https://doi.org/10.1017/CBO9781139088435.

Farrugia, D., Paolucci, E., D'Amico, S., Galea, P., 2016. Inversion of surface wave data for subsurface shear wave velocity profiles characterized by a thick buried low-velocity layer. Geophys. J. Int. 206, 1221–1231. https://doi.org/10.1093/GJI/GGW204.

Farrugia, D., Galea, P., D'Amico, S., 2021. Modelling and assessment of earthquake ground response in areas characterised by a thick buried low-velocity layer. Nat. Hazards 105, 115–136.

Foody, G.M., Warner, T.A., Nellis, M.D., 2009. The SAGE Handbook of Remote Sensing, pp. 1–568.

Gawthorpe, R.L., Hurst, J.M., 1993. Transfer zones in extensional basins: their structural style and influence on drainage development and stratigraphy. J. Geol. Soc. Lond. 150, 1137–1152. https://doi.org/10.1144/GSJGS.150.6.1137.

Gawthorpe, R.L., Leeder, M.R., 2000. Tectono-sedimentary evolution of active extensional basins. Basin Res. 12, 195–218. https://doi.org/10.1111/J.1365-2117.2000.00121.X.

Giocoli, A., Stabile, T.A., Adurno, I., Perrone, A., Gallipoli, M.R., Gueguen, E., Norelli, E., Piscitelli, S., 2015. Geological and geophysical characterization of the southeastern side of the High Agri Valley Southern Apennines, Italy. Nat. Hazards Earth Syst. Sci. 15, 315–323. https://doi.org/10.5194/NHESS-15-315-2015.

Girardeau-Montaut, D. (2016). CloudCompare. France: EDF R&D Telecom ParisTech, 11, 5.

Gold, R.D., Stephenson, W.J., Odum, J.K., Briggs, R.W., Crone, A.J., Angster, S.J., Gold, R.D., Stephenson, W.J., Odum, J.K., Briggs, R.W., et al., 2013. Concealed quaternary strike-slip fault resolved with airborne lidar and seismic reflection: the Grizzly Valley fault system, Northern Walker Lane, California. J. Geophys. Res. Solid Earth 118, 3753–3766. https://doi.org/10.1002/JGRB.50238.

Herrero, A., Improta, L., Zollo, A., Dell'Aversana, P., Morandi, S., 2000. 2-D nonlinear traveltime tomography by multi-scale search: imaging an overthrust structure in the Southern Apennines, AGU 2000 fall meeting. Eos. Trans. AGU 81 (418), 910.

Hunt, C.O., 1997. Quaternary deposits in the Maltese Islands: a microcosm of environmental change in Mediterranean Lands. GeoJournal 41, 101–109. https://doi.org/10.1023/A:1006824605544/METRICS.

Iannucci, R., Martino, S., Paciello, A., D'Amico, S., Galea, P., 2020. Investigation of cliff instability at Għajn Ħadid Tower (Selmun Promontory, Malta) by integrated passive seismic techniques. J. Seismol. https://doi.org/10.1007/s10950-019-09898-z.

Illies, J.H., 1981. Graben formation — the Maltese Islands — a case history. Dev. Geotectonics 17, 151–168. https://doi.org/10.1016/B978-0-444-41956-9.50018-6.

Improta, L., Zollo, A., Herrero, A., Frattini, R., Virieux, J., Dell'Aversana, P., 2002. Seismic imaging of complex structures by non-linear traveltime inversion of dense wide-angle data: application to a thrust belt. Geophys. J. Int. 151, 264–278. https://doi.org/10.1046/j.1365-246X.2002.01768.x.

Improta, L., Ferranti, L., De Martini, P.M., Piscitelli, S., Bruno, P.P., Burrato, P., Civico, R., Giocoli, A., Iorio, M., D'Addezio, G., et al., 2010. Detecting young, slow-slipping active faults by geologic and multidisciplinary high-resolution geophysical investigations: a case study from the Apennine seismic belt, Italy. J. Geophys. Res. Solid Earth 115, 11307. https://doi.org/10.1029/2010JB000871.

Konno, K., Ohmachi, T., 1998. Ground-motion characteristics estimated from spectral ratio between horizontal and vertical components of microtremor. Bull. Seismol. Soc. Am. 88, 228–241. https://doi.org/10.1785/BSSA0880010228.

Leucci, G., Persico, R., De Giorgi, L., Lazzari, M., Colica, E., Martino, S., Iannucci, R., Galone, L., D'Amico, S., 2021. Stability assessment and geomorphological evolution of sea natural arches by geophysical measurement: the case study of Wied Il-Mielah Window Gozo, Malta. Sustainability 13, 12538. https://doi.org/10.3390/SU132212538.

Loke, M.H., 2002. Tutorial : 2-D and 3-D Electrical Imaging Surveys.

Loke, M.H., Barker, R.D., 1996. Rapid least-squares inversion of apparent resistivity pseudosections by a Qua-si-Newton Method. Geophys. Prospect. 44, 131–152. https://doi.org/10.1111/j.1365-2478.1996.tb00142.x.

Mantovani, M., Devoto, S., Forte, E., Mocnik, A., Pasuto, A., Piacentini, D., Soldati, M., 2013. A multidisciplinary approach for rock spreading and block sliding investigation in the north-western coast of Malta. Landslides 10, 611–622.

Martinelli, M., Bistacchi, A., Balsamo, F., Meda, M., 2019. Late oligocene to pliocene extension in the Maltese Islands and implications for geodynamics of the Pantelleria rift and Pelagian platform. Tectonics 38, 3394–3415. https://doi.org/10.1029/2019TC005627.

Micallef, A., Spatola, D., Caracausi, A., Italiano, F., Barreca, G., D'Amico, S., Petronio, L., Coren, F., Facchin, L., Blanos, R., Pavan, A., Paganini, P., Taviani, M., 2019. Active degassing across the Maltese Islands (Mediterranean Sea) and implications for its neotectonics. Mar. Pet. Geol. 104, 361–374. https://doi.org/10.1016/j.marpetgeo.2019.03.033.

Molnar, S., Sirohey, A., Assaf, J., Bard, P.Y., Castellaro, S., Cornou, C., Cox, B., Guillier, B., Hassani, B., Kawase, H., et al., 2022. A review of the microtremor horizontal-to-vertical spectral ratio (MHVSR) method. J. Seismol. 26, 653–685. https://doi.org/10.1007/s10950-021-10062-9.

Moore, I.D., Gessler, P.E., Nielsen, G.A., Peterson, G.A., 1993. Soil attribute prediction using terrain analysis. Soil Sci. Soc. Am. J. 57, 443–452. https://doi.org/10.2136/sssaj1993.03615995005700020026x.

Nakamura, Y., 1989. A method for dynamic characteristics estimation of subsurface using microtremor on the ground surface. Q. Rep. Railw. Tech. Res. 30, 25–33.

Palano, M., Ferranti, L., Monaco, C., Mattia, M., Aloisi, M., Bruno, V., Siligato, G., 2012. GPS velocity and strain fields in Sicily and southern Calabria, Italy: updated geodetic constraints on tectonic block interaction in the Central Mediterranean. J. Geophys. Res. Solid Earth. 117 (B7).

Panzera, F., D'Amico, S., Lotteri, A., Galea, P., Lombardo, G., 2012. Seismic site response of unstable steep slope using noise measurements: the case study of Xemxija Bay area, Malta. Nat. Hazards Earth Syst. Sci. 12, 3421–3431. https://doi.org/10.5194/nhess-12-3421-2012.

Panzera, F., D'Amico, S., Galea, P., Lombardo, G., Gallipoli, M.R., Pace, S., 2013. Geophysical measurements for site response investigation: preliminary results on the Island of Malta. Boll. Geofis. Teor. Appl. 54, 111–128. https://doi.org/10.4430/BGTA0084.

Paolucci, E., Albarello, D., D'Amico, S., Lunedei, E., Martelli, L., Mucciarelli, M., Pileggi, D., 2015. A large scale ambient vibration survey in the area damaged by May-June 2012 seismic sequence in Emilia Romagna, Italy. Bull. Earthq. Eng. 13, 3187–3206. https://doi.org/10.1007/s10518-015-9767-5.

Pedley, H., 1993. Geological map of the Maltese Island: sheets 1, Malta Island; Sheet 2, Gozo Island.

Pedley, M., 2011. The Calabrian Stage, Pleistocene highstand in Malta: a new marker for unravelling the late Neogene and Quaternary history of the islands. J. Geol. Soc. Lond. 168, 913–926. https://doi.org/10.1144/0016-76492010-080.

Pedley, H.M., House, M.R., Waugh, B., 1976. The geology of Malta and Gozo. Proc. Geol. Assoc. 87, 325–341. https://doi.org/10.1016/s0016-787876)80005-3.

Persico, R., Muci, G., 2023. Ground penetrating radar investigation and georeferencing without global satellite navigation systems: the case history of the amphitheatre of Lecce, Italy. Geophys. Prospect. 71 (6), 1047–1055.

Persico, R., D'Amico, S., Matera, L., Colica, E., De Giorgio, C., Alescio, A., Galea, P., 2019. GPR investigations at St John's Co-Cathedral in Valletta. Near Surf. Geophys. 17 (3), 213–229. https://doi.org/10.1002/nsg.12046.

Pischiutta, M., Villani, F., D'Amico, S., Vassallo, M., Cara, F., Di Naccio, D., Rovelli, A., 2016. Results from shallow geophysical investigations in the northwestern sector of the island of Malta. Phys. Chem. Earth, Parts A/B/C 98, 41–48. https://doi.org/10.1016/j.pce.2016.10.013.

Putz-Perrier, M.W., Sanderson, D.J., 2010. Distribution of faults and extensional strain in fractured carbonates of the North Malta Graben. Am. Assoc. Pet. Geol. Bull. 94, 435–456. https://doi.org/10.1306/08260909063.

Sowers, T., Boyd, O.S., 2019. Petrologic and Mineral Physics Database for use with the U. S. Geological Survey National Crustal Model. Open-File Report, https://doi.org/10.3133/OFR20191035.

Stephenson, W.J., Odum, J.K., Williams, R.A., McBride, J.H., Tomlison, I., 2012. Characterization of intrabasin faulting and deformation for earthquake hazards in Southern Utah Valley, Utah, from high-resolution seismic imaging. Bull. Seismol. Soc. Am. 102 (2), 524–540. https://doi.org/10.1785/0120110053.

Thiele, S.T., Grose, L., Cui, T., Cruden, A.R., Micklethwaite, S., 2019. Extraction of high-resolution structural ori-entations from digital data: a Bayesian approach. J. Struct. Geol. 122, 106–115. https://doi.org/10.1016/J.JSG.2019.03.001.

Vella, A., Galea, P., D'Amico, S., 2013. Site frequency response characterisation of the Maltese Islands based on ambient noise H/V ratios. Eng. Geol. 163, 89–100. https://doi.org/10.1016/J.ENGGEO.2013.06.006.

Villani, F., Tulliani, V., Sapia, V., Fierro, E., Civico, R., Pantosti, D., 2015. Shallow subsurface imaging of the Piano Di Pezza active normal fault (Central Italy) by high-resolution refraction and electrical resistivity tomography coupled with time-domain electromagnetic Data. Geophys. J. Int. 203, 1482–1494. https://doi.org/10.1093/GJI/GGV399.

Villani, F., D'Amico, S., Panzera, F., Vassallo, M., Bozionelos, G., Farrugia, D., Galea, P., 2018. Shallow high-resolution geophysical investigation along the western segment of the Victoria Lines Fault Island of Malta. Tectonophysics 724–725, 220–233. https://doi.org/10.1016/J.TECTO.2018.01.010.

Wathelet, M., Chatelain, J.L., Cornou, C., Di Giulio, G., Guillier, B., Ohrnberger, M., Savvaidis, A., 2020. Geopsy: a user-friendly open-source tool set for ambient

vibration processing. Seismol. Res. Lett. 91 (3), 1878–1889. https://doi.org/10.1785/0220190360.